DEVELOPMENTAL BIOLOGY

The role of ipRGCs in ocular growth and myopia development

Ai-Lin Liu, Yun-Feng Liu, Ge Wang, Yu-Qi Shao, Chen-Xi Yu, Zhe Yang, Zi-Rui Zhou, Xu Han, Xue Gong, Kang-Wei Qian, Li-Qin Wang, Yuan-Yuan Ma, Yong-Mei Zhong*, Shi-Jun Weng*, Xiong-Li Yang*

The increasing global prevalence of myopia calls for elaboration of the pathogenesis of this disease. Here, we show that selective ablation and activation of intrinsically photosensitive retinal ganglion cells (ipRGCs) in developing mice induced myopic and hyperopic refractive shifts by modulating the corneal radius of curvature (CRC) and axial length (AL) in an opposite way. Melanopsin- and rod/cone-driven signals of ipRGCs were found to influence refractive development by affecting the AL and CRC, respectively. The role of ipRGCs in myopia progression is evidenced by attenuated form-deprivation myopia magnitudes in ipRGC-ablated and melanopsin-deficient animals and by enhanced melanopsin expression/photoresponses in form-deprived eyes. Cell subtype–specific ablation showed that M1 subtype cells, and probably M2/M3 subtype cells, are involved in ocular development. Thus, ipRGCs contribute substantially to mouse eye growth and myopia development, which may inspire novel strategies for myopia intervention.

INTRODUCTION

Myopia is a pathological ocular refractive condition, caused by abnormal eye growth and/or refractive power of the ocular media that renders visual images formed in front of the retina, thus resulting in blurred vision (*1*). The prevalence of myopia has steadily increased in recent years, particularly in East and Southeast Asia (*2*, *3*). This calls for the elaboration of the mechanisms controlling ocular refractive development and myopia progression. The image-forming visual system, driven mainly by rod and cone signals, is responsible for pattern vision with high spatial and temporal resolution, and it has long been implicated in the detection of image defocus, contributing substantially to emmetropization and myopia (*4*).

Rods and cones have been thought to be the only photosensitive cells in the retina for many years until the end of the past century when a novel photosensitive subset of retinal ganglion cells was identified (*5*, *6*). These cells, now named intrinsically photosensitive retinal ganglion cells (ipRGCs), are located among conventional ganglion cells and express the photopigment melanopsin (*5*, *6*). They could be driven by signals from rods and cones and project to the suprachiasmatic nucleus (SCN), the olivary pretectal nucleus (OPN), the ventral division of lateral geniculate nucleus (vLGN), and conventional visual targets such as dorsal division of lateral geniculate nucleus (dLGN) and superior colliculus (SC) (*7*, *8*). Distinct from conventional ganglion cells, ipRGCs are also activated by a melanopsin-triggered phototransduction cascade to generate spiking response (*5*).

These cells were initially thought to be responsible for modulating the so-called non–image-forming visual behaviors that occur outside of conscious visual perception, such as circadian photoentrainment and pupil constriction (*9*–*11*). In recent years, increasing evidence suggests that ipRGCs could influence image-forming vision (pattern vision) as well (*12*–*14*). Although melanopsin signaling alterations are recently implicated in experimental myopia (*15*, *16*), whether and how ipRGCs are involved in ocular growth and myopia progression is largely unknown.

In this work, we provide evidence in a mouse model to demonstrate that these cells make a considerable contribution to the establishment of the ocular refractive system. In particular, rod/cone-driven signals and melanopsin signals of ipRGCs could be responsible for controlling the corneal radius of curvature (CRC) and the axial length (AL), respectively. Moreover, ipRGC ablation reduces the magnitude of myopic shifts induced by form deprivation, which are associated with up-regulated expression of melanopsin and the stronger melanopsin-mediated light response of ipRGCs in form-deprived eyes. Among all known ipRGC subtypes, M1 cells are most likely involved in the modulation of eye growth, whereas M4 to M6 subtype cells with lower melanopsin expression seem to play a minor role. These findings also pave a new way for developing strategies for myopia intervention.

RESULTS

Targeted ablation of ipRGCs induces myopic refractive shifts

The involvement of ipRGCs in mouse refractive development was first investigated with selective ipRGC ablation using an immunotoxin, melanopsin-saporin (MEL-SAP), in which the ribosome-inactivating protein saporin is conjugated to the polyclonal melanopsin antibody UF008 (*17*). To find an appropriate dose at which a large proportion of ipRGCs was destroyed in C57BL/6 mice, but the functions of other retinal neurons were hardly affected, we evaluated the densities of UF008-labeled melanopsin immunopositive (melanopsin$^+$) cells at postinjection day 14 (D14) following intravitreal injection of MEL-SAP at three concentrations [200, 400, and 800 ng, all suspended in 0.75 μl of phosphate-buffered saline (PBS)] at postnatal day 18 (P18) (Fig. 1, A and B). As shown in Fig. 1 (C and E), the cell density was largely reduced with 200 ng of MEL-SAP, as compared to that obtained with PBS (control), and the density further declined when the dose was increased to 400 ng. With a higher dose of

State Key Laboratory of Medical Neurobiology and MOE Frontiers Center for Brain Science, Institutes of Brain Science, Fudan University, 138 Yixueyuan Road, Shanghai, China.
*Corresponding author. Email: xlyang@fudan.edu.cn (X.-L.Y.); sjweng@fudan.edu.cn (S.-J.W.); ymzhong@fudan.edu.cn (Y.-M.Z.)

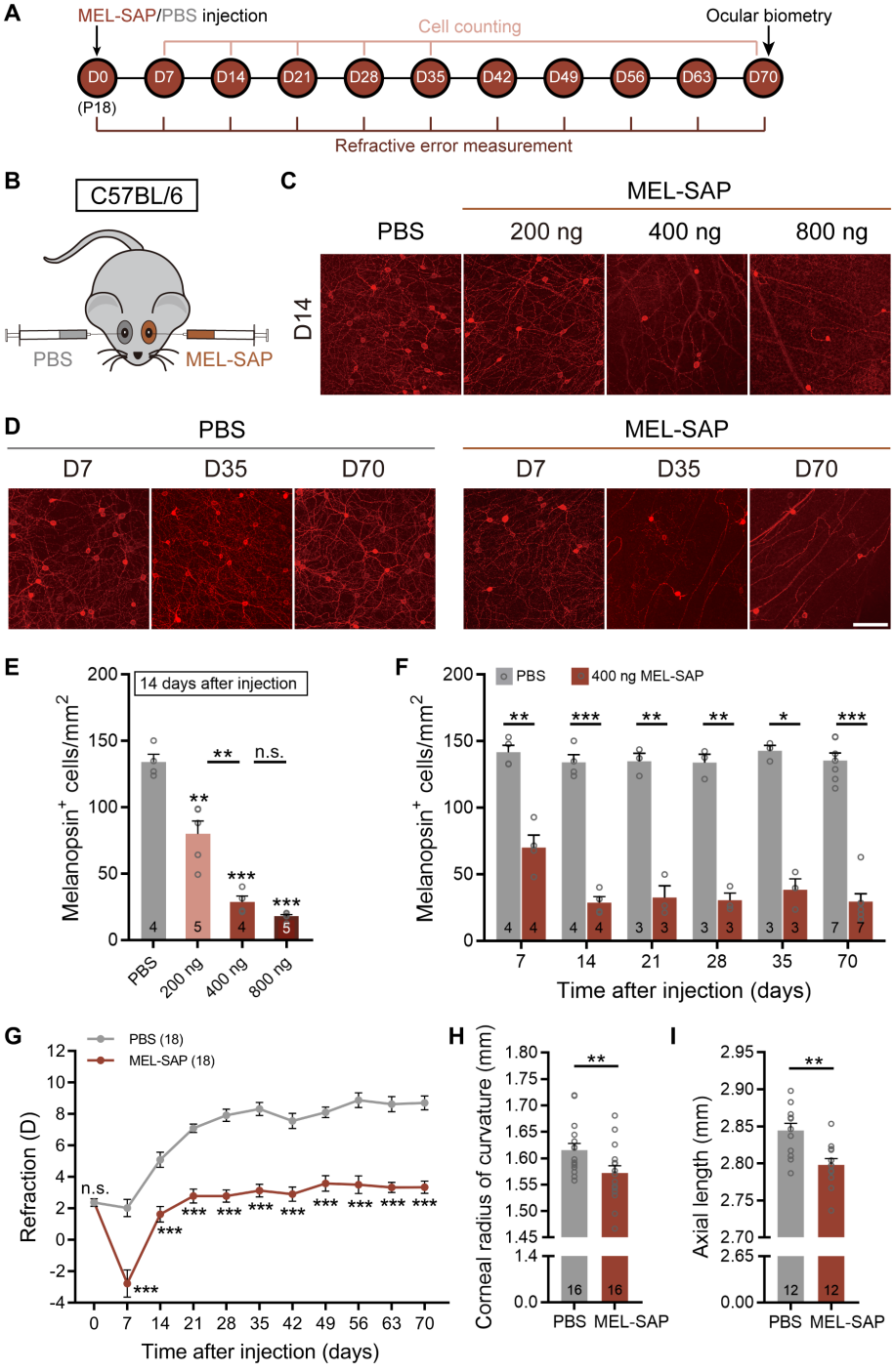

Fig. 1. IpRGC ablation induces myopic refractive shifts along with steeper corneas and shortened ALs under normal visual conditions. (**A**) Timeline of the experimental procedure and data collection. (**B**) Sketch illustration of the experimental design testing the effect of MEL-SAP–mediated ipRGC ablation on C57BL/6 mouse refractive development under normal visual conditions. (**C**) Representative photomicrographs of retinal whole mounts stained with melanopsin, which were harvested at 14 days after injection (D14) from eyes injected with PBS and different doses (200, 400, and 800 ng) of MEL-SAP. (**D**) Confocal images of whole-mount retinas, captured at different postinjection days (D7, D35, and D70), show time-dependent changes of melanopsin-immunoreactive signals in eyes injected with 400 ng of MEL-SAP and PBS. Scale bar, 100 μm. (**E**) Pooled data show a dose-dependent reduction of melanopsin$^+$ cell densities in MEL-SAP–injected eyes. Note that at D14, no significant difference was detected between 400 and 800 ng, demonstrating a saturating effect at 400 ng. (**F**) Bar chart comparing melanopsin$^+$ cell densities between 400 ng MEL-SAP– and PBS-injected eyes at various postinjection days. Note that from D14 to D70, melanopsin$^+$ cell densities in MEL-SAP–injected eyes were maintained at approximately 25% of PBS-injected eyes. (**G**) Comparisons of refractive development between 400-ng MEL-SAP–injected eyes and PBS-injected fellow eyes. MEL-SAP–injected eyes showed significantly smaller refractive errors as compared to PBS-injected eyes at all postinjection sampling points. (**H** and **I**) Bar charts summarizing the results of ocular biometric measurements conducted at D70. MEL-SAP (400 ng) reduced both the CRC (H) and AL (I) significantly. Error bars represent SEM. n.s., not significant. *$P < 0.05$, **$P < 0.01$, ***$P < 0.001$.

MEL-SAP (800 ng), the cell density was not significantly different from the value obtained at 400 ng. Figure 1 (D and F) shows the melanopsin$^+$ cell densities obtained in the eyes treated with 400 ng for different periods of time. The density dropped markedly during the first 7 days and further declined at D14, but it remained at a lower level thereafter.

Cell counting of other retinal neurons was also conducted at D14, using retinal sections and whole mounts stained immunohistochemically with molecular markers for different types of retinal cells, such as rods, cones, horizontal cells, bipolar cells, amacrine cells, non-ipRGC ganglion cells, and Müller glia. For none of the cells, significant difference in cell density was found between 400-ng MEL-SAP–injected eyes and PBS-injected fellow eyes (paired *t* test, all *P* values > 0.05; fig. S1A). In addition, also at D14, full-field electroretinograms (ERGs) were recorded, and neither the b-wave nor the a- and b-waves and oscillation potentials, evoked by dim (0.1 cd/cm^2·s, for rod dominant responses) and bright white light flashes (3 cd/cm^2·s, for mixed rod and cone responses), respectively, were significantly altered in amplitudes by 400 ng of MEL-SAP (paired *t* test, all *P* values > 0.05; fig. S1, B and C).

IpRGC loss/melanopsin deficiency is known to perturb photic regulation of circadian rhythms (*9*–*11*, *18*, *19*), which are implicated in eye growth and ocular refractive development (*20*, *21*). To rule out the possibility that monocular ipRGC ablation may cause a system-wide disruption of circadian clock regulation, wheel-running activities in monocular 400-ng MEL-SAP–injected mice were recorded under three light regimes: 12-hour light:12-hour dark (LD), constant darkness (DD), and constant light (LL). No significant changes were found in MEL-SAP–injected animals in circadian period and wheel revolutions per day under any of the three regimes, compared with PBS-injected controls (unpaired *t* test, all *P* values > 0.05; fig. S2). On the basis of these results, the dose (400 ng) was used in all experiments with MEL-SAP–induced ablation of ipRGCs throughout this work.

A cohort of C57BL/6 mice raised under normal visual environment, whose left and right eyes were respectively injected with 400 ng of MEL-SAP and equal volume of PBS at P18 (D0), was refracted weekly with an eccentric infrared photorefractor. The PBS-injected eyes displayed hyperopic shifts that increased in magnitudes with increasing time and then leveled off at D35 (Fig. 1G). The MEL-SAP–injected eyes generally underwent hyperopic development. While the two sets of data ran in parallel, MEL-SAP–injected eyes were significantly less hyperopic than PBS-injected eyes [two-way repeated-measures analysis of variance (ANOVA), $F_{1,34} = 152.1$, $P < 0.001$; Sidak multiple comparisons test, $P < 0.001$ at all postinjection sampling time points; Fig. 1G], suggesting that ipRGC loss resulted in relative myopic ocular growth.

To confirm that the effects of MEL-SAP on ipRGCs and ocular refractive development were specific, in another cohort of age-matched C57BL/6 mice, saporin fused to a nonspecific antibody [immunoglobulin G (IgG)–SAP] was monocularly injected. Injection of IgG-SAP neither caused changes in ipRGC density, as measured at D7 and D14 (paired *t* test, both $P > 0.05$; fig. S3, A and B), nor disrupted refractive development (two-way repeated-measures ANOVA, $F_{1,24} = 0.112$, $P > 0.05$; fig. S3C).

Ocular biometry was then conducted at D70 with a keratometer and a spectral-domain optical coherence tomography (SD-OCT) system. MEL-SAP caused significant changes in multiple ocular dimensions (table S1). Major changes were found in the CRC and AL. The CRC of MEL-SAP–injected eyes was significantly smaller than that of fellow control eyes (1.572 ± 0.014 mm versus 1.615 ± 0.012 mm; paired *t* test, $P < 0.01$; Fig. 1H), whereas the AL of ipRGC-ablated eyes was shorter than that of PBS-treated eyes (2.798 ± 0.009 mm versus 2.845 ± 0.010 mm; paired *t* test, $P < 0.01$; Fig. 1I). Similar changes in the CRC and AL were detected at an earlier time point, D35 (CRC, 1.494 ± 0.008 mm versus 1.569 ± 0.012 mm; AL, 2.726 ± 0.009 mm versus 2.767 ± 0.008 mm; paired *t* test, $P < 0.001$ and $P < 0.01$, respectively). Since the myopic shift caused by steeper cornea was larger in magnitude than the hyperopic shift caused by shorter AL, the resulting refractive shift was myopic.

Selective chemogenetic activation of ipRGCs induces hyperopic refractive shifts

Effects of chemogenetic activation of ipRGCs on ocular growth were also examined. The chemogenetic activator hM3Dq fused to green fluorescent protein tag (hM3Dq-GFP) was introduced into ipRGCs at P21 via monocular intravitreal injection of AAV-hSyn-DIO-hM3Dq-GFP in *Opn4*$^{Cre/+}$ mice, in which Cre recombinase, driven by the melanopsin promoter, was exclusively expressed in ipRGCs, and these mice were denoted as *Opn4*$^{Cre/+}$-hM3Dq mice (Fig. 2, A and B). Targeted expression of hM3Dq was verified by applying the same AAV vector in *Opn4*$^{Cre/+}$: Ai14 retinas, in which tdTomato fluorescent protein is specifically expressed in ipRGCs. Colocalization analysis of GFP and tdTomato, conducted at 3 weeks after viral delivery, showed that 48.38 ± 2.08% of ipRGCs expressed hM3Dq ($n = 4$), whereas almost all hM3Dq-containing cells were ipRGCs (Fig. 2C). This result is consistent with previous reports (*22*). Functional expression of hM3Dq in vivo was further verified by examining pupillary constriction, a well-established function driven by ipRGCs, in *Opn4*$^{Cre/+}$-hM3Dq mice, at 3 weeks after hM3Dq treatment. Although the animals were housed in darkness, pupillary constriction could be immediately detected after intraperitoneal injection of the hM3Dq agonist clozapine *N*-oxide (CNO; 10 mg/kg). Constriction reached a plateau at around 120 min and remained at this level for at least 6 hours, suggesting a strong, persistent activation of ipRGCs. The pupil then dilated gradually (Fig. 2, D1 and D2).

Refractive development was then examined in *Opn4*$^{Cre/+}$-hM3Dq mice. Left eyes of these animals were injected with the hM3Dq-GFP vector at P21, and 3 weeks later, the animals were housed in darkness for another 21 days with daily injections of CNO (10 mg/kg). Right eyes were injected with a GFP only–expressing virus (AAV-hSyn-DIO-GFP) as control (Fig. 2A). Weekly refraction measurements revealed that hM3Dq-infected eyes became more hyperopic, compared to fellow eyes at all three time points following CNO injection (paired *t* test, all *P* values < 0.001; Fig. 2E). Ocular dimensional assessment conducted at P63 (table S2) showed that the CRC of hM3Dq-infected eyes was larger than that of fellow control eyes (1.584 ± 0.006 mm versus 1.569 ± 0.007 mm; paired *t* test, $P < 0.05$; Fig. 2F), while the AL of hM3Dq-infected eyes was longer than that of control virus–treated eyes (2.780 ± 0.011 mm versus 2.753 ± 0.010 mm; paired *t* test, $P < 0.05$; Fig. 2G). These changes were in a direction opposite to those obtained in mice with ipRGC ablation (Fig. 1, H and I).

Melanopsin signals promote ocular axial elongation

IpRGCs are activated by rod/cone-driven synaptic inputs and by signals due to melanopsin activation. Melanopsin signals are known to play an important role in a variety of ipRGC-mediated physiological

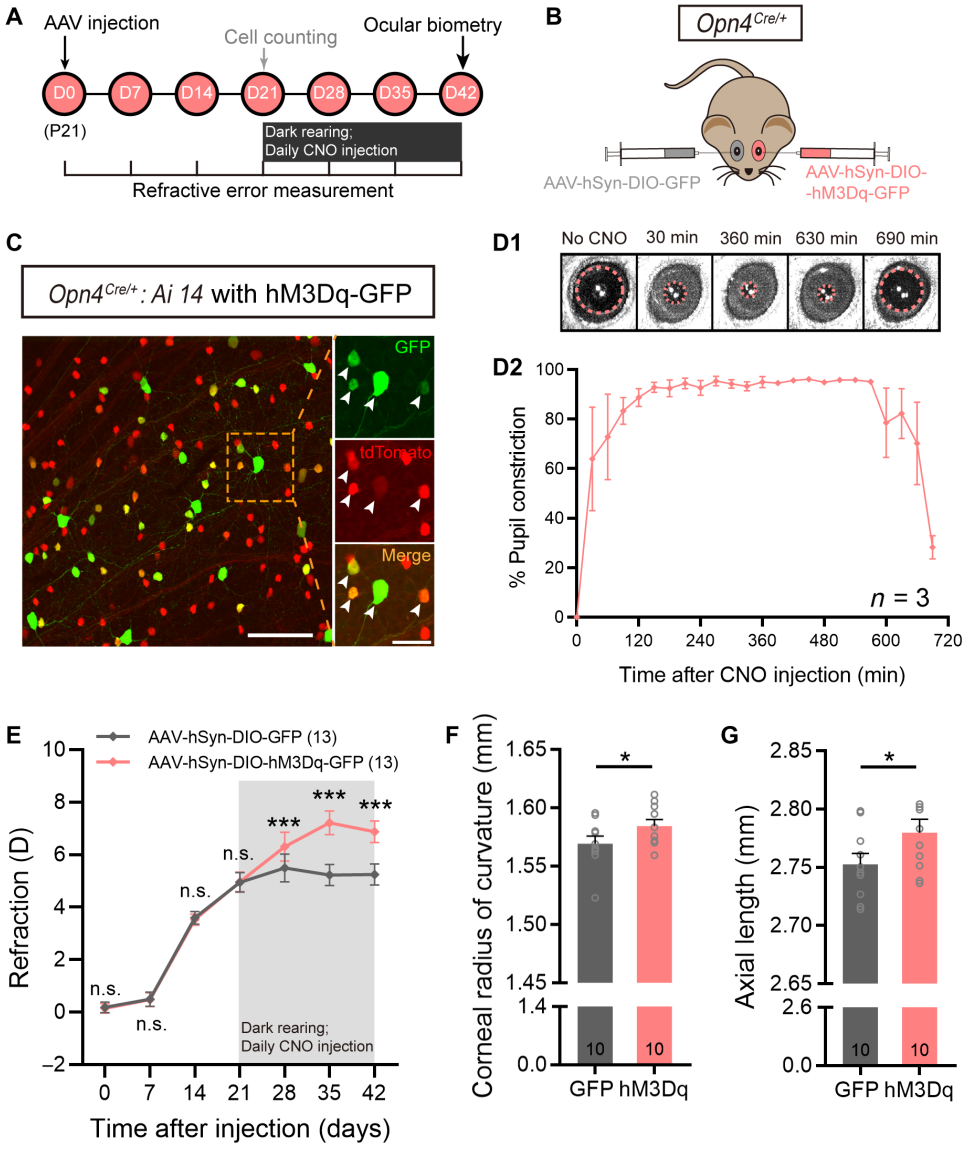

Fig. 2. Chemogenetic activation of ipRGCs causes hyperopic growth. (**A**) Experimental procedures and data collection pipeline. (**B**) Scheme of intravitreal delivery of AAV-hSyn-DIO-hM3Dq-GFP to *Opn4*$^{Cre/+}$ mice. Fellow eyes were injected with AAV-hSyn-DIO-GFP as control. (**C**) Representative photomicrograph of a retinal whole mount harvested from an *Opn4*$^{Cre/+}$:Ai14 mouse at 21 days after AAV-hSyn-DIO-hM3Dq-GFP injection. All hM3Dq-infected cells exhibiting fluorescence of GFP tag (arrows) were tdTomato-labeled ipRGCs. Scale bars, 100 μm (left) and 40 μm (right). (**D1**) Representative pupil images of an hM3Dq-infected *Opn4*$^{Cre/+}$ mouse housed in complete darkness. Images were captured before and at 30, 360, 630, and 690 min after intraperitoneal CNO injection (10 mg/kg). (**D2**) Percent of pupil constriction, calculated from the baseline pupil area before CNO treatment, as a function of time after CNO injection in hM3Dq-infected *Opn4*$^{Cre/+}$ mice. (**E**) Comparison of refraction growth curves between hM3Dq-infected eyes and control virus–infected fellow eyes in *Opn4*$^{Cre/+}$ mice. Before CNO treatment, the refractive errors were rather comparable between the two eyes. However, after the animals were housed in darkness and injected with CNO, hM3Dq-infected eyes, in which ipRGCs were selectively activated, were significantly more hyperopic compared to fellow eyes at all three sampling time points. (**F** and **G**) Bar charts summarizing the results of ocular biometric measurements conducted at 21 days after daily CNO administration. hM3Dq-infected eyes had significantly larger CRC (F) and significantly longer AL (G) as compared to fellow eyes. Error bars represent SEM. *P < 0.05, ***P < 0.001.

functions, usually distinct from those of rod/cone-driven signals (*23*, *24*). To demonstrate the role of melanopsin signals in ocular growth, we took advantage of the *Opn4*$^{Cre/Cre}$ mouse (Fig. 3, A and B), in which both copies of melanopsin-coding genes were replaced by Cre-coding sequences (*25*), virtually leading to melanopsin knockout (Fig. 3C). Figure 3D shows the refractive development of these mice and their wild-type littermates (WTs), both with normal visual experience, as a function of age. Although both genotypes underwent hyperopic development from P21 to P63, the refractive errors of *Opn4*$^{Cre/Cre}$ mice measured at all postnatal time points were invariably greater than those of WTs (two-way repeated-measures ANOVA, $F_{1,27}$ = 75.79, P < 0.05; Sidak multiple comparisons test, P < 0.001 at all sampling time points), indicating that melanopsin absence induced hyperopic eye growth. Ocular parameter measurement data attained at P63 (see table S3) revealed that the CRC of *Opn4*$^{Cre/Cre}$ mice was indistinguishable from that of WTs (1.583 ± 0.007 mm

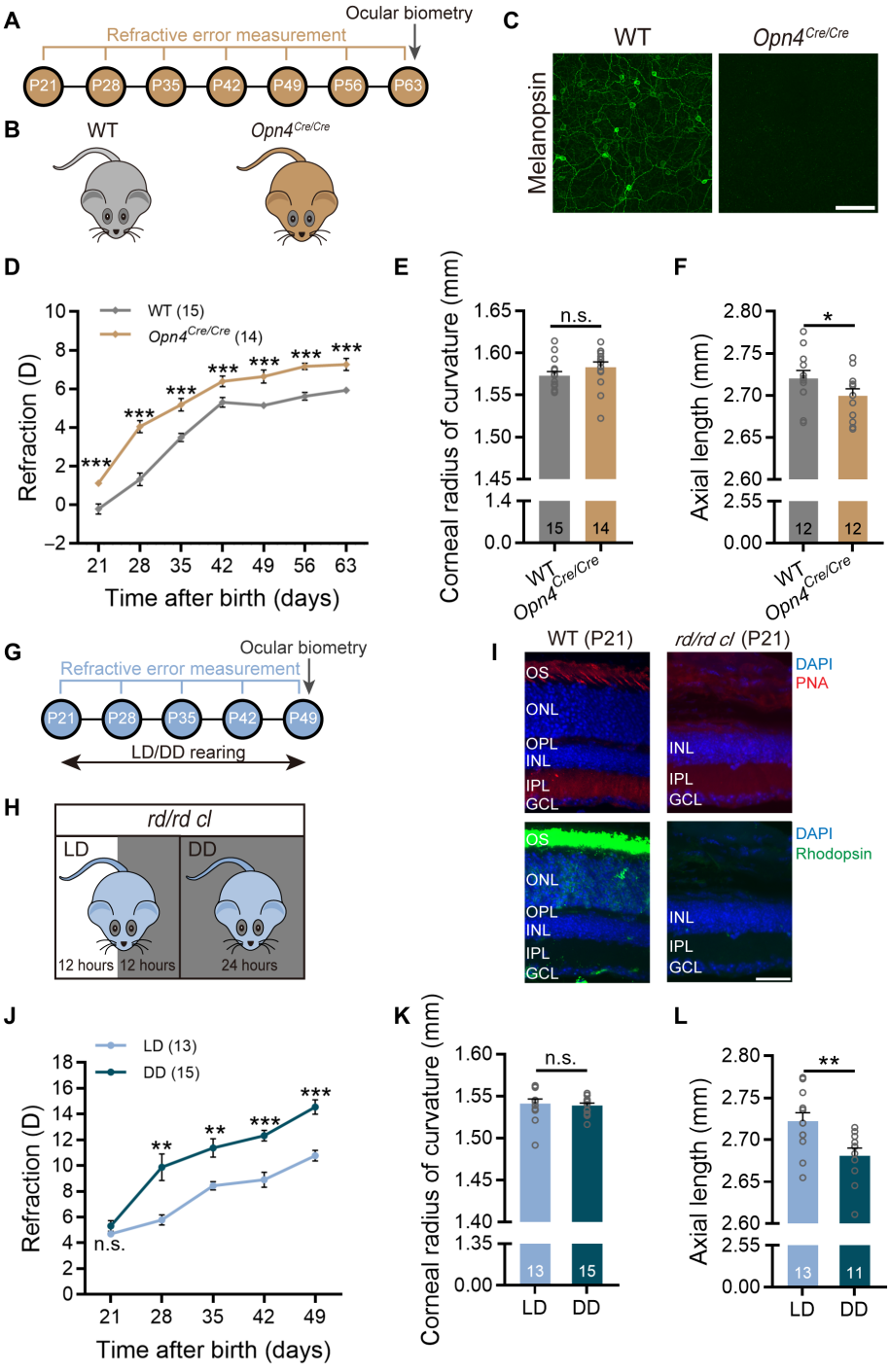

Fig. 3. Melanopsin signals contribute to axial ocular development. (**A**) Flowchart showing data collection time points of the experiments conducted on *Opn4*$^{Cre/Cre}$ mice. (**B**) Diagram of *Opn4*$^{Cre/Cre}$ and breed-matched WT mice. (**C**) Confirmation of lack of melanopsin-immunoreactive signals in the *Opn4*$^{Cre/Cre}$ retina. Scale bar, 100 μm. (**D**) Comparison of refractive development growth curves revealed a significant upward scaling in refraction, corresponding to hyperopic shift, in *Opn4*$^{Cre/Cre}$ mice as compared to WTs. Note that the refractive errors obtained at different postnatal days in *Opn4*$^{Cre/Cre}$ mice were all larger than those in WTs over a 42-day period starting at P21. (**E** and **F**) Ocular parameter assessment carried out at P63 revealed no appreciable difference in the CRC between the two genotypes (E), but significantly shortened AL was detected in *Opn4*$^{Cre/Cre}$ mice (F). (**G**) Flowchart showing procedure and data collection time points of the *rd/rd cl* mouse experiments. (**H**) Schematic demonstration of raising *rd/rd cl* mice under different light conditions (from P21 to P49): LD (12-hour light:12-hour dark cycle) and DD (constant darkness). (**I**) Immunohistochemical staining for rods (rhodopsin) and cones (PNA) verified the absence of outer retinal photoreceptors in P21 *rd/rd cl* mice. Scale bar, 40 μm. DAPI, 4′,6-diamidino-2-phenylindole. (**J**) Refractive development growth curves of LD- and DD-raised *rd/rd cl* mice. LD-raised animals, in which melanopsin signals were activated for 12 hours daily, were significantly more myopic as compared to DD-raised ones at all four sampling time points after P21. (**K** and **L**) Bar charts summarizing the results of ocular parameter measurements performed at P49. The CRC was similar between the two groups housed in different light regimes (K), whereas the AL of the LD group was significantly larger than that of the DD group (L). Error bars represent SEM. *$P < 0.05$, **$P < 0.01$, ***$P < 0.001$.

versus 1.573 ± 0.005 mm; unpaired *t* test, $P > 0.05$; Fig. 3E). However, axial growth in *Opn4*$^{Cre/Cre}$ mice was much slower than that in WTs (2.696 ± 0.008 mm versus 2.725 ± 0.009 mm; unpaired *t* test, $P < 0.05$; Fig. 3F). Highly comparable results were obtained in *Opn4*$^{-/-}$ mice, in which tau-lacZ was targeted into the melanopsin gene locus, thus abolishing melanopsin expression (fig. S4) (*6*, *26*).

The contribution of melanopsin to refractive development was also examined in *rd/rd cl* mice (Fig. 3, G and H), in which all rods and cones were lost at P21 (Fig. 3I) (*27*) so that ipRGCs were solely driven by melanopsin signals. These mice were divided into two groups: "LD group" received 12-hour normal illumination daily to allow melanopsin activation, whereas "DD group" was kept in complete darkness for 24 hours daily, thus lacking melanopsin signals (Fig. 3H). While both groups exhibited hyperopic development across age, the LD group showed much less hyperopia compared to the DD group throughout development (two-way repeated-measures ANOVA, $F_{1,26} = 43.47$, $P < 0.001$; Sidak multiple comparisons test, $P < 0.01$ at P28 and P35, $P < 0.001$ at P42 and P49; Fig. 3J). Such a relative myopic shift had an axial origin, since ocular biometry carried out at P49 (data summarized in table S4) revealed that the AL in the LD group was significantly larger than that in the DD group (2.722 ± 0.010 mm versus 2.681 ± 0.009 mm; unpaired *t* test, $P < 0.01$; Fig. 3L). No statistical difference in the CRC was detected between the two groups (1.541 ± 0.006 mm versus 1.539 ± 0.003 mm; unpaired *t* test, $P > 0.05$; Fig. 3K). Together with the data from melanopsin knockout animals (Fig. 3, A to F), these results suggest that melanopsin signals make a substantial contribution to axial elongation during visually guided eye growth.

To understand the contribution of rod/cone-driven signals of ipRGCs in ocular refractive development, the melanopsin-deficient mouse (*Opn4*$^{Cre/Cre}$) was used again (Fig. 4, A and B). Since there were only rod/cone-driven signals, ipRGC ablation by intravitreal injection of AAV-CAG-DIO-DTA was equivalent to the abolishment of rod/cone-driven signals of these cells. Because ipRGCs in *Opn4*$^{Cre/Cre}$ mice could not be immunolabeled by melanopsin antibodies, the ipRGC ablation efficiency of this approach was instead evaluated in *Opn4*$^{Cre/Cre}$*: Ai14* mice in which ipRGCs also lacked melanopsin but could be visualized by tdTomato fluorescence. Under our conditions, the ablation efficiency of AAV-CAG-DIO-DTA was around 70% at D21 (Fig. 4, C and D), quite comparable to that achieved by 400 ng of MEL-SAP in C57BL/6 mice (78%; Fig. 1, E and F).

We then ran refraction measurements on DTA virus–injected *Opn4*$^{Cre/Cre}$ animals weekly before (D0) and after injection (D7 to D42). Just as seen in MEL-SAP–injected eyes, a myopic shift was detected in DTA virus–injected eyes versus control virus–injected fellow eyes across time (two-way repeated-measures ANOVA, $F_{1,40} = 238.5$, $P < 0.001$; Sidak multiple comparisons test, $P < 0.001$ at all postinjection sampling time points; Fig. 4E). However, ocular biometry performed at D42 (data are summarized in table S3) showed that, as compared to control fellow eyes, the CRC in DTA virus–injected

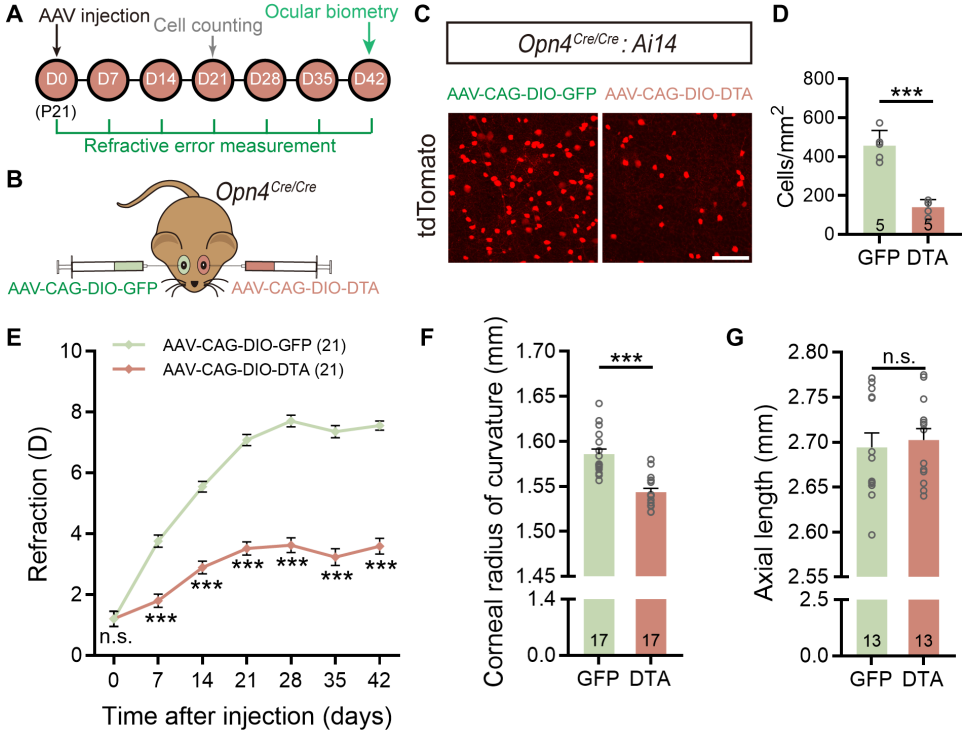

Fig. 4. Rod/cone-driven signals mediate ipRGC contribution to corneal development in normal visual environment. (**A**) Flow diagram of experimental procedure and data collection. (**B**) Schematic illustration of ipRGC ablation in *Opn4*$^{Cre/Cre}$ mice by intravitreal administration of AAV-CAG-DIO-DTA (DTA virus). Fellow eyes were injected with AAV-CAG-DIO-GFP (control virus) for comparison. (**C**) Representative confocal images of whole-mount *Opn4*$^{Cre/Cre}$: Ai14 retinas captured at D21 after DTA virus and control virus injection. Scale bar, 100 μm. (**D**) Grouped data show that tdTomato-labeled ipRGCs in DTA virus–injected *Opn4*$^{Cre/Cre}$: Ai14 retinas were significantly fewer as compared to those in control virus–injected ones. (**E**) Change in refractive error as a function of postinjection time of *Opn4*$^{Cre/Cre}$ mice housed in normal visual conditions. Note that DTA virus–injected eyes were significantly more myopic than control virus–injected fellow eyes at all sampling time points over a 42-day period. (**F** and **G**) Ocular dimension measurements conducted at D42 revealed that the CRC was significantly reduced in DTA virus–injected eyes as compared to that in control virus–injected eyes (F), whereas the AL was similar between two eyes (G). Error bars represent SEM. ***$P < 0.001$.

eyes was smaller (1.543 ± 0.004 mm versus 1.586 ± 0.006 mm; paired *t* test, $P < 0.001$; Fig. 4F), but the AL was quite comparable (2.702 ± 0.013 mm versus 2.694 ± 0.016 mm; paired *t* test, $P > 0.05$; Fig. 4G and table S3). These results strongly suggest that rod/cone-driven signals of ipRGCs are specifically responsible for controlling CRC development.

IpRGCs contribute substantially to myopia development

Since ipRGCs contribute to ocular axial development, it seems reasonable to predict that myopia, a refractive condition commonly associated with excessive axial elongation (*2*, *3*), may be modulated by signals from ipRGCs. To evaluate the role of ipRGCs in form-deprivation myopia (FDM) development, we examined the changes in refractive shifts after ipRGCs were ablated by MEL-SAP (Fig. 5, A and B). To avoid the complexity that could be invoked by possible nonlinear summation of the effects of MEL-SAP and form deprivation, intravitreal injections of MEL-SAP were made to both eyes; then, monocular form deprivation was applied on the left eye for 4 weeks. Although FDM could still be induced, the myopic shifts induced by form deprivation were found to be significantly smaller in magnitudes in these ipRGC-ablated mice, as compared to those in control mice with binocular PBS injection [−3.354 ± 0.267 diopters (D) versus −4.825 ± 0.213 D; unpaired *t* test, $P < 0.001$; Fig. 5, C and D], suggesting that FDM development was somehow suppressed in ipRGC-ablated eyes.

The biometric data, summarized in table S1, further show that the AL, obtained at P53, of deprived eyes was longer than that of fellow

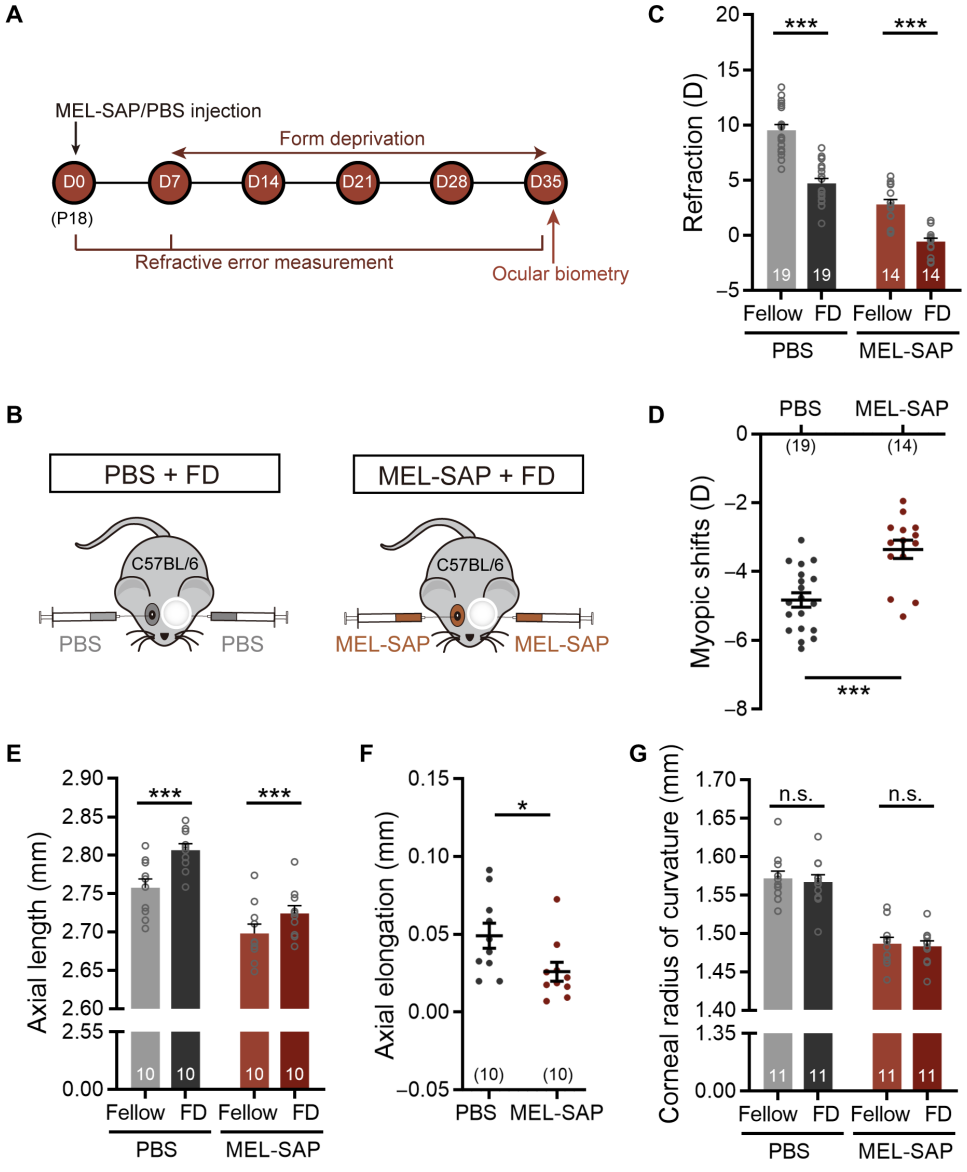

Fig. 5. IpRGCs make a significant contribution to FDM. (**A**) Experimental procedures and data collection flow diagram. (**B**) Scheme of C57BL/6 mice with binocular PBS or 400 ng of MEL-SAP injections at P18 (D0) and 4-week monocular form deprivation starting at P25 (D7). (**C**) Bar charts summarizing refractions of deprived eyes and fellow eyes in ipRGC-ablated and control animals after 4-week form deprivation. In both groups, deprived eyes were significantly more myopic relative to fellow eyes. (**D**) Pooled data show that the myopic shifts induced in ipRGC-ablated mice were significantly reduced as compared to those in control mice. (**E**) In both groups, the AL in deprived eyes was significantly longer than that in fellow eyes. (**F**) Axial elongation in ipRGC-ablated mice was significantly smaller than that in control mice. (**G**) Bar chart shows that the CRC was similar between deprived and fellow eyes in both groups. Error bars represent SEM. **P* < 0.05, ****P* < 0.001.

eyes, regardless of whether ipRGCs were ablated by MEL-SAP or not (paired *t* test, both $P < 0.001$; Fig. 5E). However, the axial elongation was lesser when ipRGCs were ablated (0.026 ± 0.006 mm versus 0.049 ± 0.008 mm for intact ipRGCs; unpaired *t* test, $P < 0.05$; Fig. 5F), suggesting that ipRGC ablation attenuated FDM by slowing axial growth. Meanwhile, it should be emphasized that the CRC was unchanged by form deprivation (paired *t* test, both $P > 0.05$; Fig. 5G). Together, these results suggest that ipRGCs contribute to the retinal processing of degraded images, which potentiates myopia progression by causing excessive axial growth.

Melanopsin signals are a major factor in ipRGC-mediated myopia progression

Since melanopsin signals play an essential role in normal axial eye growth (Figs. 3 and 4), we speculated that these signals may play a similar role in myopia progression. The speculation was confirmed. Refractive shifts and axial elongation induced by 4-week form deprivation were determined at P63 in $Opn4^{Cre/Cre}$ mice (Fig. 6, A and B), and both of them were smaller in magnitudes than those in WT mice (refractive shifts: −2.064 ± 0.163 D in $Opn4^{Cre/Cre}$ mice versus −4.287 ± 0.086 D in WT mice; unpaired *t* test, $P < 0.001$; Fig. 6, C and D; axial elongation: 0.016 ± 0.003 mm in $Opn4^{Cre/Cre}$ mice versus 0.033 ± 0.005 mm in WT mice; unpaired *t* test, $P < 0.01$; Fig. 6, E and F). Similar results were obtained in another melanopsin knockout strain ($Opn4^{-/-}$) (fig. S5, A to E), strongly suggesting an important role of melanopsin signals in myopia progression. This suggestion is further strengthened by examining changes in myopic shifts when the white lighting environment, used for raising the animals, was modified by a notch filter (approximately 460- to 500-nm band stop), which affected melanopsin-based ipRGC activity (λmax = 480 nm) to a greater extent, but reduced rod/cone activities to a much lesser extent. FDM C57BL/6 mice raised under this 480 nm–blocking lighting environment showed smaller myopic shifts and axial elongation induced by 4-week form deprivation, as compared to mice treated with white lighting environment (fig. S5, F to J).

To further explore whether melanopsin signals or rod/cone-driven signals were differentially involved in ipRGC-mediated myopia progression, monocular form deprivation was conducted on bilateral AAV-CAG-DIO-DTA–treated $Opn4^{Cre/Cre}$ mice (Fig. 6, G and H). Myopic refractive shifts of comparable magnitudes were seen in these mice and control virus–treated $Opn4^{Cre/Cre}$ mice (−2.164 ± 0.102 D versus −2.270 ± 0.219 D; unpaired *t* test, $P > 0.05$; Fig. 6, I and J). Consistently, form deprivation–induced AL changes were also indistinguishable between the two aforementioned $Opn4^{Cre/Cre}$ mouse groups (0.012 ± 0.003 mm versus 0.015 ± 0.002 mm, unpaired *t* test; $P > 0.05$; Fig. 6, K and L). Thus, rod/cone-driven inputs of ipRGCs play a minor role in FDM development.

Changes in melanopsin signals in FDM mice

The involvement of melanopsin signals in myopia development raised the possibility that these signals may change in myopic eyes. In 4-week form-deprived C57BL/6 animals, we failed to find any significant differences in whole-retina melanopsin$^+$ cell densities (125.87 ± 3.11 cells/mm^2 versus 122.11 ± 3.46 cells/mm^2; paired *t* test, $P > 0.05$; Fig. 7, C and D), or in melanopsin$^+$ cell densities obtained from any of the four retinal quadrants (paired *t* test, $P > 0.05$ for all quadrants; Fig. 7D), between deprived eyes and fellow eyes, although there were approximately 5-D myopic shifts between them (Fig. 7, A and B). Meanwhile, real-time quantitative polymerase chain reaction (PCR) showed that melanopsin transcript levels were comparable between retinas harvested from deprived and fellow eyes (paired *t* test, $P > 0.05$; Fig. 7E). We further tested melanopsin protein levels by quantitative Western blot analysis using the PA1-780 melanopsin antibody, revealing two bands at approximately 53 and 85 kDa, corresponding to the molecular weights of unglycosylated and glycosylated melanopsin, respectively (Fig. 7F) (*28*). Densitometric analysis showed that optical densities of the two bands from deprived eyes were significantly higher than those from fellow eyes (paired *t* test, $P < 0.05$ for unglycosylated, $P < 0.01$ for glycosylated; Fig. 7G), suggesting an up-regulation of melanopsin expression in myopic eyes.

Next, a high-throughput evaluation of melanopsin-initiated light responses was conducted by using multielectrode array (MEA) technique. During these experiments, all glutamatergic inputs were blocked by adding a glutamatergic blocker cocktail containing L-AP4 (50 μM), DNQX (40 μM), ACET (2 μM), and D-AP5 (30 μM) to the bath solution. In dark-adapted retinas, a series of 10-s 480-nm light flashes (3.42×10^{11} to 1.51×10^{15} photons cm^{-2} s^{-1}) elicited sluggish but very persistent spike discharges in a few MEA channels, typical of melanopsin-based phototransduction. Similar to previous studies (*29*, *30*), in retinas from both deprived and fellow eyes, the light-induced spike discharges increased as a function of flash intensity. Representative raster plots of these responses are shown in Fig. 7H. Plotting of irradiance-response (I-R) curves of melanopsin-based responses showed that the light-evoked spike numbers during 10-s light flashes were significantly increased (two-way repeated-measures ANOVA, $F_{1,135} = 4.717$, $P < 0.05$, Sidak multiple comparisons test, $P < 0.05$ at 1.51×10^{15} photons cm^{-2} s^{-1}; Fig. 7I), while the peak latencies of the responses were significantly reduced (two-way repeated-measures ANOVA, $F_{1,135} = 8.058$, $P < 0.01$; Sidak multiple comparisons test, $P < 0.05$ at 3.42×10^{14} photons cm^{-2} s^{-1}, $P < 0.001$ at 1.51×10^{15} photons cm^{-2} s^{-1}; Fig. 7J), in deprived eyes as compared to those in fellow eyes. These results indicate that melanopsin-driven signals are enhanced during myopia progression.

M1 ipRGCs and their retrograde inputs to dopaminergic amacrine cells contribute to refractive development

Last, we conducted a series of experiments to identify the ipRGC subtype(s) that modulates ocular growth in mice. The myopic shifts observed in MEL-SAP–treated C57BL/6 mice (Fig. 1) indicated the involvement of M1 to M3 ipRGC subtypes, because MEL-SAP is based on the UF008 melanopsin antibody, which primarily recognizes these three subtypes with relatively higher melanopsin levels (*31*). This was further confirmed by unchanged densities of the somata labeled by SMI-32, a marker for M4 cells, in MEL-SAP–injected eyes (104.57 ± 5.39 cells/mm^2 versus 124.82 ± 11.86 cells/mm^2; paired *t* test, $P > 0.05$; fig. S6, A and B). At D14, in a separate cohort of 400-ng MEL-SAP–injected C57BL/6 mice, we harvested the retinas and stained them with another melanopsin antibody, PA1-780, which preferentially targets M1 cells (*32*). In PBS-injected control eyes, as expected, somata positive for PA1-780 were sparser than those positive for the UF008 antibody (Figs. 1C and 8A). The densities of PA1-780–positive cells were reduced by ~70% (13.58 ± 2.47 cells/mm^2 versus 63.56 ± 5.36 cells/mm^2; paired *t* test, $P < 0.001$; Fig. 8B) by MEL-SAP, an extent similar to that of the UF008-labeled cells (Fig. 1, E and F). These results confirmed the severe ablation of M1 cells in MEL-SAP–treated eyes and suggested that M1 to M3 cells were equally ablated.

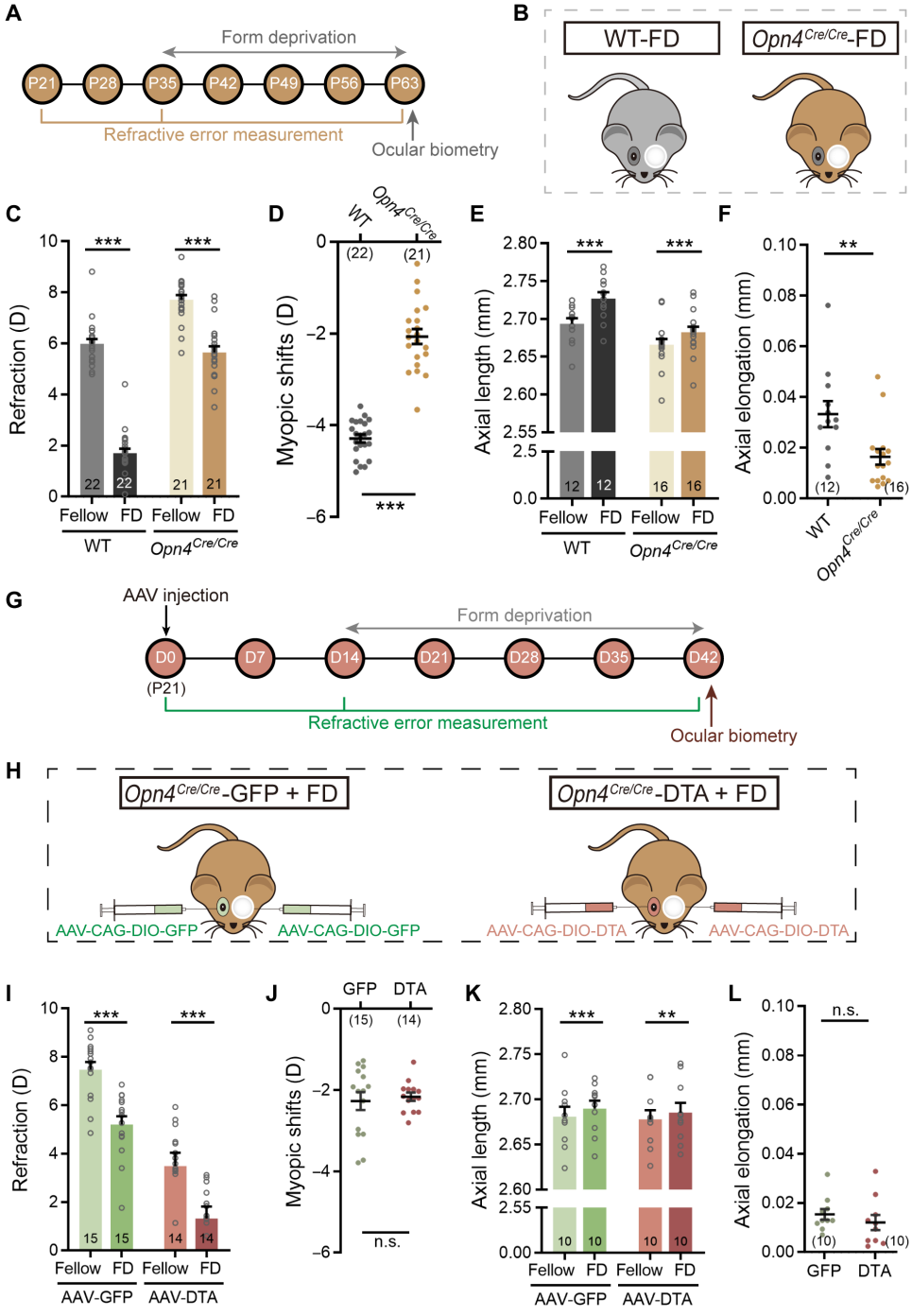

Fig. 6. Melanopsin signals mediate ipRGC contribution to FDM by promoting axial growth. (**A**) Procedure/data collection timeline for the experiments shown in (B) to (F). (**B**) Schematic illustration of WT (left) and *Opn4*$^{Cre/Cre}$ mice (right); starting at P35, mice were form-deprived on left eyes for 4 weeks. (**C**) Form deprivation induced significant myopic shifts in deprived eyes as compared to fellow eyes in both WTs and *Opn4*$^{Cre/Cre}$ mice. (**D**) The myopic shifts induced in *Opn4*$^{Cre/Cre}$ mice were significantly smaller than those in WT mice. (**E**) In both genotypes, the AL of deprived eyes was significantly larger than that of fellow eyes. (**F**) The axial elongation in *Opn4*$^{Cre/Cre}$ mice was significantly smaller as compared to WT mice. (**G**) Procedure and data collection pipeline of the experiments conducted on AAV-injected *Opn4*$^{Cre/Cre}$ mice. (**H**) Schematic illustration of dividing *Opn4*$^{Cre/Cre}$ mice into two groups: one binocularly injected with control virus (AAV-CAG-DIO-GFP, left), and the other binocularly injected with AAV-CAG-DIO-DTA (right); both groups were treated with 4-week monocular form deprivation starting at D14 (P35). (**I**) In both groups, refractive errors in deprived eyes were significantly smaller than those in fellow eyes, suggesting a myopic shift. (**J**) Grouped data show that no significant difference in deprivation-induced myopic shifts was detected between DTA and control virus–injected *Opn4*$^{Cre/Cre}$ mice. (**K**) The AL of deprived eyes was significantly larger than that of fellow eyes in both groups. (**L**) The axial elongation in DTA virus–injected *Opn4*$^{Cre/Cre}$ mice was comparable to that in control virus–treated *Opn4*$^{Cre/Cre}$ mice after 4-week form deprivation. Error bars represent SEM. $^{**}P < 0.01$, $^{***}P < 0.001$.

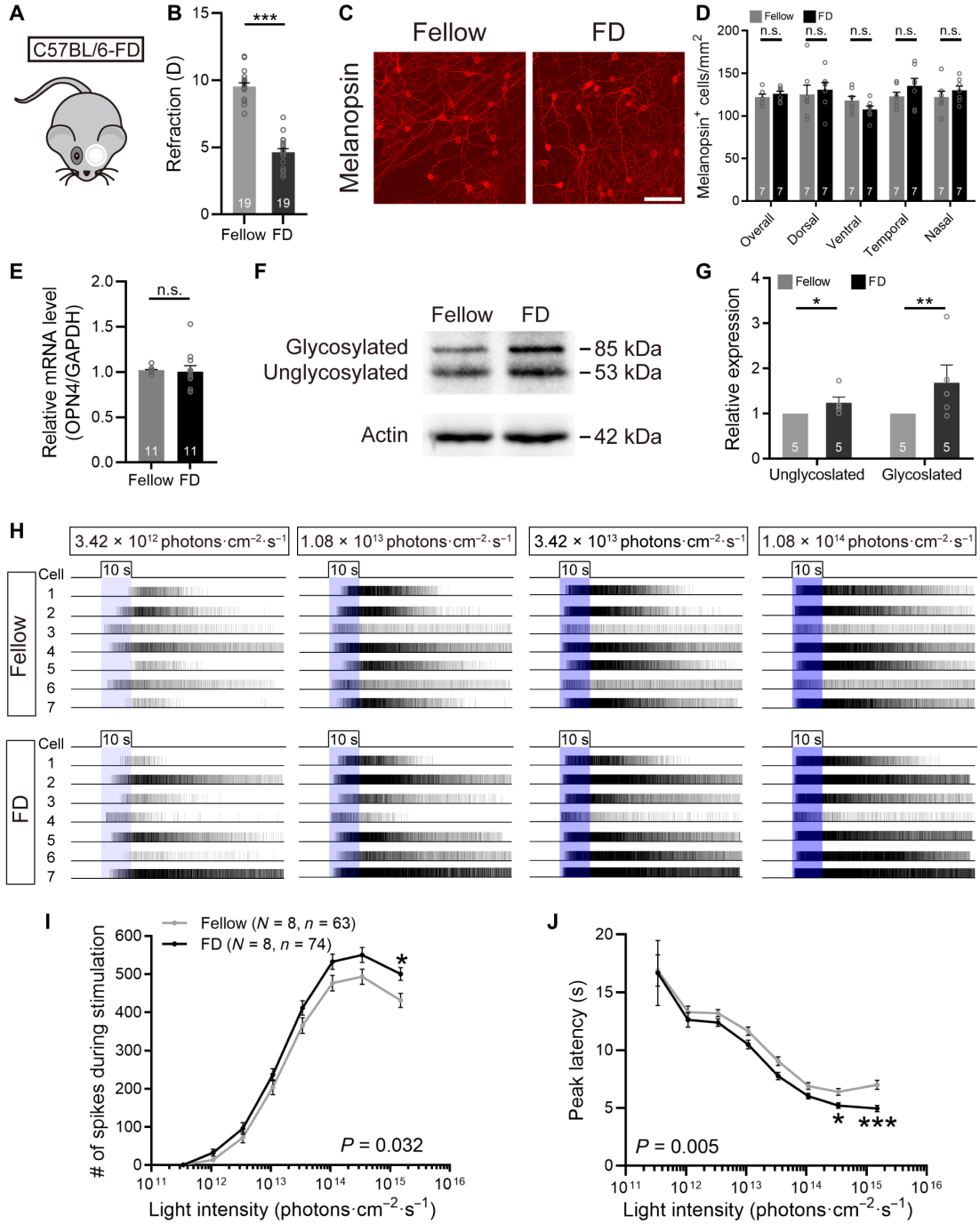

Fig. 7. FDM is associated with alterations in melanopsin phototransduction. (**A**) Schematic diagram of FDM induction in C57BL/6 mice by 4-week monocular occluder wear. (**B**) Bar chart shows that form deprivation induced significant myopic shifts in refraction in deprived eyes relative to fellow eyes. (**C**) Representative photomicrographs of melanopsin-stained retinal whole mounts harvested from deprived and fellow eyes. Scale bar, 100 μm. (**D**) The overall densities of melanopsin$^+$ cells, and those calculated separately from four retinal quadrants, were all indistinguishable between deprived and fellow eyes. (**E**) Melanopsin mRNA levels were not altered by 4-week form deprivation as revealed by quantitative reverse transcription PCR (qRT-PCR). (**F**) Representative photographs of Western blots of whole-retina homogenates extracted from deprived and fellow eyes for the PA1-780 melanopsin antibody. (**G**) Densitometric analysis revealed that levels of whole-retina melanopsin, in both glycosylated and unglycosylated forms, were significantly increased in deprived eyes compared to fellow eyes. (**H**) Representative raster plots of melanopsin-based light-evoked spiking activity obtained via MEA recording on a whole-mount retina harvested from a fellow eye (top) and another retina from a deprived eye (bottom). The light stimulation was a series of full-field, 480-nm light pulses presented in increasing intensity (blue bars). Each trace represents the spike train from a distinguishable, single unit identified by offline cluster analysis. Photoresponses were recorded in the presence of the glutamatergic cocktail and typical of melanopsin-based activity, being sluggish and persistent. (**I** and **J**) Group data comparing I-R functions of two major parameters (total spike number during stimulation, peak latency) of melanopsin-based light responses between deprived and fellow eyes. Note that melanopsin-based responses in deprived eyes exhibited significantly increased total spike number (I) and significantly reduced peak latency (J) as compared to those in fellow eyes. Error bars represent SEM. *$P < 0.05$, **$P < 0.01$, ***$P < 0.001$.

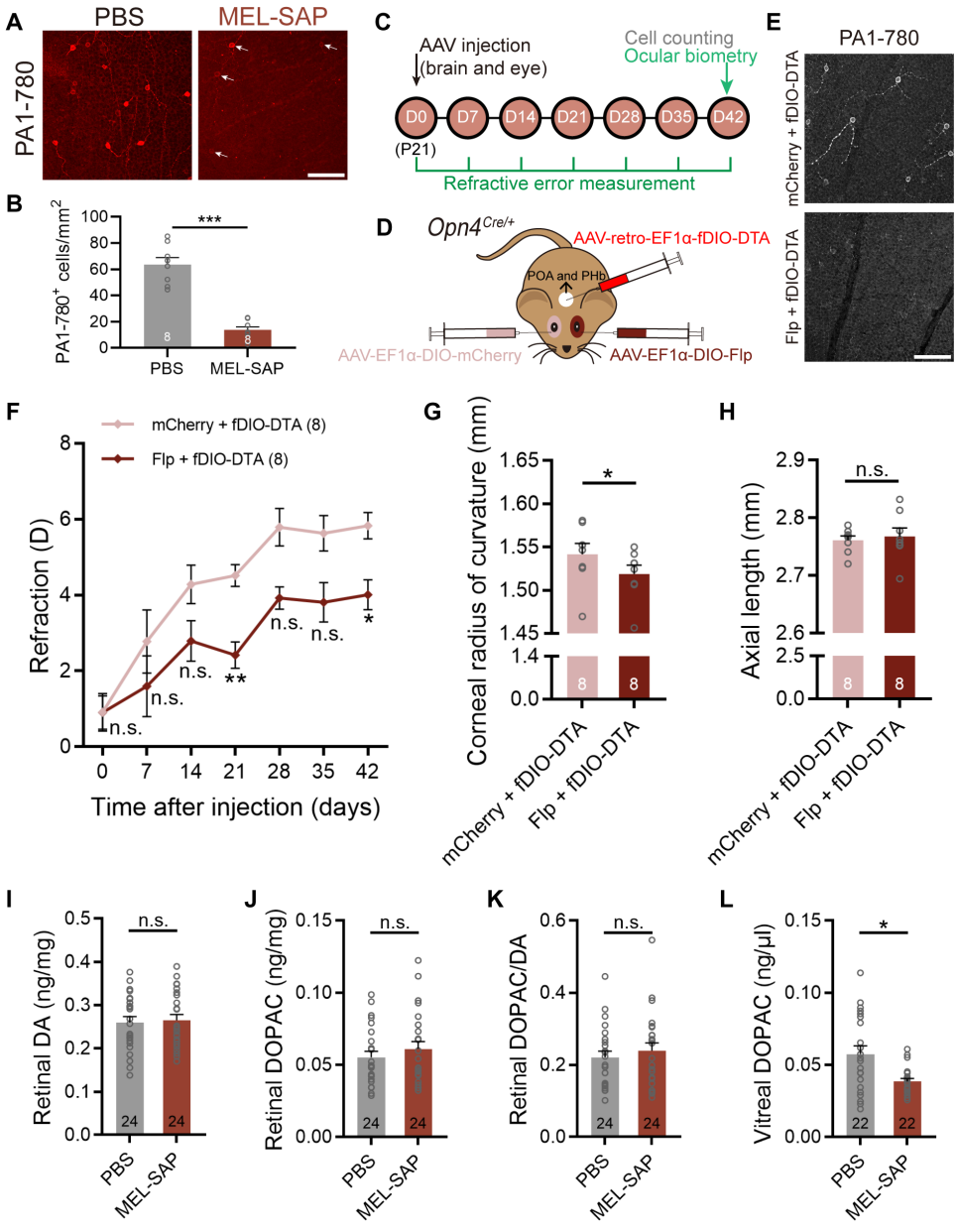

Fig. 8. IpRGC contribution to ocular development is accounted for by M1 cells and associated with reduced DA release. (**A** and **B**) Representative microscopic images and pooled data showing a significant (~70%) reduction in the density of somata positive to the PA1-780 melanopsin antibody, which preferentially labels M1-type ipRGCs, in 400-ng MEL-SAP–treated C57BL/6 retinas. Arrows point to a few residual PA1-780–labeled cells. Scale bar, 100 μm. (**C**) Timeline of the procedure and data collection of the dual virus injection experiment. (**D**) Schematic illustration of selective M1 cell ablation in *Opn4*$^{Cre/+}$ mice by intravitreal injection of AAV-EF1α-DIO-Flp and stereotaxic injection of an Flp-dependent DTA-coding retrograde virus (AAV-retro-EF1α-fDIO-DTA) to the POA and PHb, two nuclei to which ipRGC projections are predominantly from M1 cells. Fellow eyes were injected with AAV-EF1α-DIO-mCherry (control virus) for comparison. (**E**) Confocal micrographs showing that fDIO-DTA/DIO-Flp treatment significantly reduced PA1-780–positive signals in the *Opn4*$^{Cre/+}$ retina, confirming the severe ablation of M1 cells. Scale bar, 100 μm. (**F**) The growth curve of refraction of M1 cell–ablated eyes showed a significant myopic shift as compared to that of control virus–injected fellow eyes. (**G** and **H**) Bar charts summarizing the results of ocular biometric measurements conducted at D42. M1 cell ablation significantly reduced the CRC (G) but did not change the AL (H). (**I** to **L**) Bar charts summarizing the results of HPLC analysis on samples harvested at D42. IpRGC ablation did not show appreciable effects on retinal DA (I) or DOPAC levels (J), nor did it alter the retinal DOPAC/DA ratio (K); however, it reduced vitreal DOPAC levels, an indicator of retinal DA release, significantly (L). Error bars represent SEM. *$P < 0.05$, **$P < 0.01$, ***$P < 0.001$.

To selectively ablate M1 cells, we used a dual-virus strategy in P21 *Opn4*$^{Cre/+}$ mice by intravitreal injection of a Cre-dependent virus (AAV-EF1α-DIO-Flp) that expresses Flp recombinase, in combination of stereotaxic delivery of an Flp-dependent retrograde virus encoding DTA (AAV-retro-EF1α-fDIO-DTA) to the preoptic area (POA) and perihabenular nucleus (PHb) (Fig. 8, C and D), two brain areas to which ipRGC axon projections are predominantly from M1 cells (*33*, *34*). At D21, immunostaining of whole-mount retinas

revealed that PA1-780–positive signals were significantly reduced in Flp virus–treated eyes compared to control virus–injected fellow eyes, confirming the successful ablation of M1 cells (Fig. 8E).

Mouse eyes with M1 cell ablation showed a significant myopic refractive shift relative to control virus–injected fellow eyes across development (two-way repeated-measures ANOVA, $F_{1,14} = 20.09$, $P < 0.001$; Sidak multiple comparisons test, $P < 0.01$ at D21, $P < 0.05$ at D42; Fig. 8F). This result provided direct evidence that M1 cells contribute significantly to refractive development. Moreover, the AL was quite comparable between M1 cell–ablated and control eyes at D42 (2.768 ± 0.015 mm versus 2.761 ± 0.008 mm; paired *t* test, $P > 0.05$; Fig. 8H). However, the CRC of M1 cell–ablated eyes was markedly reduced (1.519 ± 0.010 mm versus 1.542 ± 0.013 mm; paired *t* test, $P < 0.05$; Fig. 8G), which might account for the observed myopic shift. Thus, the shortened AL in MEL-SAP–injected eyes (Fig. 1I) was likely caused, at least in part, by the ablation of M2 and/or M3 cells.

Retinal dopamine (DA) is implicated in visually guided eye growth in various species (*35*, *36*). M1 ipRGCs provide intraretinal "retrograde" signals to dopaminergic amacrine cells (DACs) (*37*), the sole retinal neurons releasing DA. Recent studies show that reducing retinal DA levels leads to myopic eye growth with a shortened CRC in mice (*38*, *39*), an effect similar to that seen in ipRGC-ablated animals. In 400-ng MEL-SAP–injected eyes, high-performance liquid chromatography (HPLC) analysis revealed that the levels of vitreal 3,4-dihydroxyphenylacetic acid (DOPAC, the major metabolite of DA), a robust indicator of retinal DA release, were significantly lower than those of control eyes (0.039 ± 0.002 ng/μl versus 0.057 ± 0.006 ng/μl; paired *t* test, $P < 0.05$; Fig. 8L), suggesting that the malfunction of DACs may be a mechanism underlying the refractive development alterations in ipRGC-ablated eyes, although steady levels of retinal DA, DOPAC, and DOPAC/DA turnover rate were all similar between MEL-SAP– and PBS-injected eyes (paired *t* test, all $P > 0.05$; Fig. 8, I to K).

To evaluate the role of M4 to M6 cells, we compared refractive development between two groups of $Opn4^{Cre/+}$ mice: one monocularly injected with 400 ng of MEL-SAP so that M1 to M3 cells were preferentially ablated, and the other injected with AAV-CAG-DIO-DTA to indiscriminately ablate M1 to M6 cells (fig. S6C). Both MEL-SAP–injected eyes and DTA-injected eyes exhibited less hyperopic refractive error compared with PBS- or control virus–injected fellow eyes across ages (fig. S6, D and E). Moreover, the magnitudes of myopic shifts were virtually indistinguishable between these two groups (two-way repeated-measures ANOVA, $F_{1,8} = 0.12$, $P > 0.05$; Sidak multiple comparisons test, $P > 0.05$ at all sampling time points; fig. S6F). Thus, M4 to M6 cells seemingly play a relatively minor, if any, role in mouse ocular growth.

DISCUSSION

Involvement of ipRGCs in ocular refractive development and FDM formation

A major finding in this study is that ipRGCs are substantially involved in ocular refractive development in mice, which is crucial for image-forming visual functions. This conclusion is derived from the considerable myopic refractive shifts induced in the eyes when most ipRGCs were ablated (Fig. 1), yet they exhibited hyperopic shifts when ipRGCs were selectively activated (Fig. 2). Given the involvement of ipRGCs in modulating ocular refractive development, it was not surprising that 4-week form deprivation induced much less myopic shifts in ipRGC-ablated animals (Fig. 5). Accordingly, axial elongation, induced by form deprivation in $Opn4^{Cre/Cre}$ mice, was significantly shorter than that of WT mice (Fig. 6). The reduced magnitude of myopic shifts obtained in melanopsin knockout eyes could be attributed to the contribution of ipRGCs to visually guided ocular growth, which was evidently mediated by melanopsin signals of ipRGCs. This was supported by the fact that the myopic shifts obtained in form-deprived $Opn4^{Cre/Cre}$ mice remained almost unchanged when ipRGCs were ablated by AAV-CAG-DIO-DTA (Fig. 6). In other words, just as seen in the experiments concerning the effects on ocular development, it is melanopsin signals of ipRGCs, but not rod/cone-driven ones, that influence myopia progression. These results provide strong evidence, suggesting that ipRGCs make a considerable contribution to both ocular refractive development and FDM progression, thus creating a new dimension in exploring possible mechanisms underlying myopia progression. While making the revision of this work, Chakraborty *et al.* (*40*) published a related paper in which some of the major results related to refractive errors and myopic shifts induced by form deprivation are not in line with our study. In particular, $Opn4^{DTA/DTA}$ mice, an analog of our MEL-SAP–treated mice with ipRGC ablation, were more hyperopic, and the myopic shifts caused by form deprivation were larger, rather than smaller, as compared to control mice. Possibly accounting for the difference, there are several methodological differences between the two studies, such as the techniques used to ablate ipRGCs, the time lengths of form deprivation, and control group assignments. As far as control group assignments are concerned, it should be emphasized that, in the present study, control experiments were conducted on either vehicle/control virus–injected fellow eyes, vehicle/control virus–injected animals of exactly the same strain as the experimental animals, or WTs. Further work is needed to reconcile the discrepancies between the studies.

The particular ipRGC subtype(s) involved in mouse refractive development

To date, a total of six subtypes (M1 to M6) of ipRGCs have been identified in mice according to distinct soma-dendritic profiles and physiological properties (*7*, *41*). Chemogenetically induced hyperopic eye growth in the $Opn4^{Cre/+}$ mouse (Fig. 2) could be due to the activation of any of the six ipRGC subtypes, because Cre-dependent transgene expression shows no bias toward particular subtype(s) (*22*, *42*). However, MEL-SAP–induced myopic refractive shifts (Fig. 1) were likely caused by the loss of M1 to M3 ipRGCs, because MEL-SAP is based on the UF008 melanopsin antibody, which primarily recognizes M1 to M3 cells with relatively higher melanopsin levels (*25*). Furthermore, our "dual virus" experiment showed that selective ablation of M1 cells was adequate to induce myopic eye growth by reducing the CRC (Fig. 8), strongly suggesting a substantial role of M1 cells in mouse ocular development. M1 cells have the highest levels of melanopsin among all subtypes (*43*), the deficiency of which causes retinal clock gene dysfunction (*44*); their processes co-fasciculate with DACs in the outermost inner plexiform layer (*45*), thus being structurally possible to directly modulate retinal dopaminergic functions; moreover, their dendrites exhibit close spatial relationship with the intermediate capillary plexus (*32*), which facilitates melanopsinergic regulation of retinal blood vessels.

Among the non-M1 subtypes, M4 to M6 ipRGCs were unlikely involved, not only because of the significantly lower melanopsin expression (so that melanopsin knockout is probably a minor effect to

them, not enough to cause the phenotypes in melanopsin knockout mice) but also due to the observation that M1 to M6 cell ablation caused almost the same effect on refractive development as M1 to M3 cell ablation (fig. S6). By contrast, the phenotypes caused by M1 cell–selective ablation were not exactly the same as those caused by M1 to M3 cell ablation by MEL-SAP (Figs. 1 and 8): When only M1 cells were ablated, the myopic shifts were smaller, but a shortened AL, a significant effect by M1 to M3 cell ablation, was not seen. These differences indicate the involvement of M2 and/or M3 cells in mouse refractive development.

Melanopsin signals and rod/cone-driven signals of ipRGCs are associated with the AL and CRC, respectively, in normal refractive development

Signals from ipRGCs could be either rod/cone-driven or melanopsin-mediated (*46*). The second major finding of this work was that two ocular major parameters, the CRC and AL, are respectively modulated by rod/cone-driven signals and melanopsin signals of ipRGCs. The supposition that melanopsin signals are responsible for modulating the AL was supported by the following two experimental results. First, in $Opn4^{Cre/Cre}$ mice, in which melanopsin is virtually knocked out, the AL was much shorter than that of WTs, while the CRC was indistinguishable (Fig. 3). Second, in *rd/rd cl* mice, a relative myopic shift was obtained in the LD group, compared to the DD group, and such a shift was associated with axial elongation. This implies that the activation of melanopsin (as occurred in the LD group) may induce myopic shifts by modulating the AL.

Rod/cone-driven signals of ipRGCs seem to work for another function (modulating the CRC). When ipRGCs are excited, the effects of these two signals on ocular refractive states may interplay with each other, thus providing a versatile modulatory mechanism, which could be used for developing novel strategies for myopia intervention—that is, if melanopsin signals could be appropriately suppressed to reduce axial elongation, say by using melanopsin suppressant on the one hand, and to enlarge the CRC (cornea flattening) by illumination with appropriate spectral compositions to specifically activate rod/cone-driven signals of ipRGCs on the other hand. Refractive shifts produced by these approaches tend to slow down the course of myopia progression and/or to reduce the severity of myopia. One of the recent widely accepted approaches for inhibiting myopia in children is to expose them to ambient light of high levels (*47*). The effectiveness of this approach has been confirmed in human and animal models (*48*, *49*), but seems hard to reconcile with our finding that activation of melanopsin, which is activated by bright ambient light, promotes axial eye growth. However, rod/cone (especially cone) photoreceptors could also be strongly excited by bright light, thereby trigger signaling cascades for slowing down axial eye growth, which overrides the axial elongation by melanopsin. In principle, one way to improve this approach is to use light with a well-designed spectral composition so to excite rods and cones more, but to avoid activating melanopsin. In contrast, it is possible in human trials by using light of long-wavelength (>600 nm) regimes to activate red-sensitive cones well, but melanopsin much less.

Among all ipRGC subtypes, only M1 cells send intraretinal signals to DACs, a key factor associated with refractive status (*35*, *36*), by centrifugal synapses (*37*, *50*). Rod/cone signals are capable of exciting DACs via the retrograde pathway from M1s (*37*, *51*). Therefore, loss of rod/cone inputs might significantly attenuate the synaptic drive from M1 cells to DACs, thus reducing light-evoked DA release. Consistently, we found that ipRGC ablation by MEL-SAP, apparently reducing M1 cell–routed rod/cone drive to DACs, resulted in a markedly decreased retinal DA release (Fig. 8L). Depleting retinal DA results in myopic shifts in mice by shortening the CRC (*38*, *39*), a phenotype similar to that observed in M1 cell–ablated mice (Figs. 1 and 8). All these available data strongly suggest that rod/cone signals regulate corneal growth by a specialized M1 cell–DAC route, while melanopsin, expressed by all six subtypes, contributes mainly to axial elongation.

Possible mechanisms underlying ipRGC contribution to ocular growth

Convergent evidence reveals melanopsin expression in the cornea (*52*, *53*). However, our results found it unlikely that corneal melanopsin directly modulates developmental changes of the corneal curvature, in that melanopsin knockout only induced AL shortening, but did not cause appreciable changes in the CRC (Fig. 3, E and F). Instead, the CRC seems to be modulated by the rod/cone inputs to ipRGCs (Fig. 4). Thus, melanopsin expressed in the cornea is likely to exert functions other than shaping its curvature.

It is still unclear how melanopsin and rod/cone signals, both routed through ipRGCs, differentially influence the AL and CRC. Initially, we had hypothesized that M1 cells, which are of higher melanopsin expression levels, affect the AL, while M2/M3 cells, which are mainly driven by rod/cone inputs, are responsible for the CRC. But such a hypothesis was eventually rejected, because M1 cell–specific ablation did not change the AL; instead, it caused corneal steepening (Fig. 8).

The complex structural-functional interaction between M1 cells and DACs (*37*, *50*, *51*, *54*), as mentioned above, is very likely one of the mechanisms underlying ipRGC contribution to ocular growth. In addition to this study (Fig. 8), a recently published paper also reported abnormal ocular DA/DOPAC levels in ipRGC-ablated animals (*40*). In wild-type C57BL/6 mice, development of experimental myopia is not associated with altered retinal DA levels (*55*). However, Chakraborty *et al.* (*40*) found that retinal DA and DOPAC levels were reduced in form-deprived mice with melanopsin deficiency, but melanopsin knockout itself does not change retinal DA levels (*40*, *56*). Thus, an intact ipRGC-DAC interplay seems indispensable for mouse refractive development. Future studies are needed to more explicitly explore roles of this local circuit. Second, the effects of ipRGCs on refractive development may be mediated by their impacts on ocular circadian rhythms, which are essential for normal emmetropization (*20*, *21*). In addition to innervating the master biological clock, the SCN, and controlling rhythmic activities systematically, ipRGCs are known to regulate "local" intraretinal rhythms, as evidenced by the attenuation of daily variation in cone ERG (*57*) and the disruption of clock gene rhythms in mice lacking melanopsin (*44*). Photoresponses of ipRGCs, the earliest light-evoked activity in the developing retina (*58*), show fluctuations in amplitude in a circadian manner (*59*), which could be passed onto neighboring cells via robust gap junction coupling (*60*) and axon collaterals (*37*), thus modulating ocular growth rhythms. Third, ipRGC contribution to ocular growth may also be associated with its intensive interaction with retinal blood vessels. A fraction of ipRGC processes is anatomically adjacent to the intermediate capillary plexus (*32*). It is recently shown that melanopsin mediates light-driven relaxation in blood vessels (*61*). Moreover, in rats with oxygen-induced retinopathy, a condition manifested by abnormal retinal arteries, the CRC

and AL are both reduced (*62*), just as observed in MEL-SAP–treated animals (Fig. 1). Examining whether ameliorating blood perfusion could reverse the refractive changes in these mice would provide insight into the role of ipRGC–blood vessel interaction in ocular growth.

MATERIALS AND METHODS

Animals

Animals were reared and treated in accordance with the Association for Research in Vision and Ophthalmology Statement for the Use of Animals in Ophthalmic and Vision Research; all operations were approved by the Animal Care and Use Committees of Fudan University. Mice were maintained under a 12-hour light:12-hour dark cycle at an ambient illumination of approximately 200 lux during the daytime with abundant food and water. C57BL/6 mice were purchased from Shanghai Xipu'er-bikai Experimental Animal Co. Ltd. (China). *Opn4*$^{Cre/Cre}$ and *Opn4*$^{Cre/+}$ mice, which were both provided by S. Hattar (National Institute of Mental Health), were on a mixed background (C57BL/6; 129SvJ) originally, but mated for >6 generations to C57BL/6 mice. *Opn4*$^{-/-}$ (mixed C57BL/6; 129SvJ background) and *rd/rd cl* (mixed C57BL/6; C3H/He background) mice were gifts from T. Xue (University of Science and Technology of China). All genetic mice were maintained in breeding colonies at Fudan University.

Induction of form-deprivation myopia

The procedure of FDM induction has been previously described in detail (*55*). In brief, handmade translucent occluders were attached to the fur around left eyes by glue at P25 (for MEL-SAP–injected mice), P35 (for *Opn4*$^{Cre/Cre}$ mice), or P21 (for the remaining strains). A plastic collar was fitted around the neck to prevent the mice from removing the occluders. Mice wearing occluders and collars were raised in the cage singly for 4 weeks.

Specific ablation and chemogenetic activation of ipRGCs

After mice were deeply anesthetized by intraperitoneal injection of 0.6% pentobarbital sodium (10 μl/g body weight), reagents were injected into the vitreous through the temporal part of the sclera using a Nanoject II microinjector (3-000-205/206, Drummond Scientific Company, USA) with a glass micropipette (tip size, 10 to 30 μm). For immunotoxic ablation of ipRGCs in C57BL/6 mice, different doses (200, 400, and 800 ng) of MEL-SAP (IT-44, Advanced Targeting Systems, USA), all suspended in 0.75 μl of 0.1 M PBS (pH7.4), were injected at P18; control eyes received the same volume of PBS or 400 ng of nonspecific antibody–conjugated saporin (IgG-SAP, also in 0.75 μl of PBS). For selective chemogenetic activation of ipRGCs in *Opn4*$^{Cre/+}$ mice, 2 μl of AAV-hSyn-DIO-hM3Dq-GFP (BrainVTA, China) was intravitreally injected at P21; control eyes were injected with 2 μl of AAV-hSyn-DIO-GFP (BrainVTA). Three weeks later, these mice were maintained in darkness and treated with intraperitoneal injection of CNO (BrainVTA, 10 mg/kg body weight) daily to trigger hM3Dq-mediated excitation. For selective ablation of ipRGCs in *Opn4*$^{Cre/Cre}$ mice, 2 μl of AAV-CAG-DIO-DTA (BrainVTA), which enables Cre-dependent expression of diphtheria toxin gene A chain (DTA), was intravitreally injected at P21, while control eyes received equal volume of AAV-CAG-DIO-GFP (BrainVTA). All viral vectors used were at a titer of >2×10^{12} viral genome (vg)/ml.

Refractive error measurements

Refractive errors were measured as previously described (*55*), with an eccentric infrared photorefractor designed by Schaeffel *et al.* (*63*), which is customized for the mouse eye and calibrated regularly. The refractive error of each eye was averaged from three measurements. To minimize nonspecific effects, any mice with an initial interocular refractive difference of >2 D were abandoned in this study.

Ocular biometric measurements

A custom-made, ultra-long depth, SD-OCT system with a resolution at 10 μm was used to measure axial components including corneal thickness (CT), anterior chamber depth (ACD; from the posterior corneal surface to the anterior lens surface), lens thickness (LT), vitreous chamber depth (VCD; from the posterior lens surface to the vitreous-retina interface), and AL (from the anterior corneal surface to the vitreous-retina interface) as previously reported (*39*). Briefly, mice were anesthetized with a mixture of 0.6% pentobarbital and 0.2% xylazine (10 μl/g body weight) and then positioned on a stage in front of a modified slit lamp and scanned along the optical axis of the eye with an X-Y cross-scanning system. The raw SD-OCT data were exported and analyzed using custom-designed software to yield the values of axial components. CRC was measured with a keratometer (OM-4, Topcon, Japan) as previously described (*39*). The keratometer was equipped with a +20-D achromatic doublet lens and was calibrated by a series of stainless steel ball bearings (diameters from 2.318 to 4 mm). For both SD-OCT and photokeratometry, the mean value of the results of three measurements was used for further comparisons and analysis.

Immunohistofluorescence

Tissue preparation

Mice were enucleated immediately after sacrifice by 25% ethyl carbamate (10 μl/g body weight). Eyeballs were then placed in 0.01 M PBS, and the cornea, lens, and vitreous were quickly removed, leaving the retina in the posterior eyecup. For retinal sections, the eyecups were fixed for 30 min with 4% paraformaldehyde (PFA) and then chilled in 10%, 20%, and 30% (w/v) sucrose in 0.1 M phosphate buffer (pH7.4) at 4°C sequentially. The eyecups embedded in optimal cutting temperature compound (Leica, Germany) were frozen by liquid nitrogen and then sectioned vertically at 14-μm thickness on a freezing microtome (Leica). The sections were collected on gelatin-chromium–coated slides and stored at −20°C. For whole mounts, the retinas were dissected from the pigment epithelium and sclera gently, and four radial cuts were made to flatten the retina and to divide the retina into four quadrants (i.e., dorsal, ventral, temporal, and nasal). The retinas were then attached to a piece of filter paper (AABP02500, Millipore, USA) with ganglion cell side up and fixed with 4% PFA for 20 min.

Retinal staining

Retinal sections were fetched from −20°C and rinsed in 0.01 M PBS, and then the sections were blocked in 0.1 M PBS containing 6% normal donkey serum and 0.2% Triton X-100 for 2 hours at room temperature, washed in 0.01 M PBS for 3 × 15 min, and incubated with the primary antibodies in a buffer [3% normal donkey serum, 1% bovine serum albumin (BSA), and 0.2% Triton X-100 in 0.1 M PBS] for 2 days at 4°C. For retinal whole mounts, the staining procedure was the same as that of sections, but the blocking solution was made by mixing 6% normal donkey serum and 1% Triton X-100 in 0.1 M PBS, while the solution for antibody incubation was 0.1 M PBS containing 3% normal donkey serum, 1% BSA, and 1% Triton X-100.

Antibodies

The primary antibodies/cellular markers used are listed as follows: goat anti-Brn3a (Santa Cruz Biotechnology, 31984, 1:1000), mouse anti-calbindin (Swant, 300, 1:1000), mouse anti-CRALBP (Abcam, ab15051, 1:1000), mouse anti–HPC-1 (Sigma-Aldrich, S0664, 1:500), mouse anti-rhodopsin (Chemicon, MAB5356, 1:500), rhodamine-conjugated peanut agglutinin (PNA; Vector Laboratories, RL-1072-5, 1:500), rabbit anti-melanopsin [Advanced Targeting Systems, AB-N39 (UF008), 1:10,000], rabbit anti-melanopsin (Thermo Fisher Scientific, PA1-780, 1:500), mouse anti–SMI-32 (Covance, SMI32R, 1:1000), and sheep anti-Chx10 (Abcam, ab16141, 1:1000). Alexa Fluor 488/555/647–conjugated fluorescent secondary antibodies raised in donkey were obtained from Thermo Fisher Scientific (USA) or Jackson ImmunoResearch (USA) and used with a final dilution at 1:200.

Microscopic imaging and cell counting

Images of retinal sections were obtained using a 60× oil-immersion objective lens [numerical aperture (NA) 1.42] of a Fluoview FV1000 confocal microscope (Olympus Corporation, Japan). In each section, cell counting, carried out with ImageJ software (https://imagej.nih.gov/ij/), was done in a 211-μm length area located at 1.2 to 1.6 mm from the optic nerve head. Images of retinal whole mounts were acquired with a Fluoview FV1000 confocal microscope or with an Axioskop 40 fluorescence microscope (Carl Zeiss Inc., Germany) under 20× objective lenses (NA 0.75 and 0.80, respectively). Eight 520 μm–by–520 μm areas (centered at 0.6 and 1.5 mm from the optic nerve head in four quadrants) of each whole mount were imaged, and cell counting was conducted with ImageJ.

Real-time quantitative reverse transcription PCR

After mice were sacrificed, retinas were harvested, and total RNA (200 ng) was extracted and reverse-transcribed with commercially available kits (Takara Bio Inc., Japan). Quantitative real-time PCR was performed using TB Green Premix Ex Taq II (Takara Bio) on the Applied Biosystems QuantStudio 3 96-Well 0.2-mL Block. The primer sequences of OPN4 and glyceraldehyde 3-phosphate dehydrogenase (GAPDH) were 5′-TCTGTTAGCCCCACGACATC-3′ (forward) and 5′-TGAACATGTTTGCTGGTGTCC-3′ (reverse), and 5′-TGGTGAAGGTCGGTGTGAACG-3′ (forward) and 5′-AGGGGTCGTTGATGGCAACAA-3′ (reverse), respectively.

Western blot analysis

Western blot analysis was performed as previously described (*32*). In brief, total cellular proteins of retinas were extracted with a protein extraction kit (K268-50; BioVision, USA). Protein concentrations were determined using a standard bicinchoninic acid assay kit (23235, Thermo Fisher Scientific, USA). Equivalent amounts of freshly extracted retinal lysate (50 μg per lane) were electrophoresed in 10% SDS–polyacrylamide gel electrophoresis and then transferred to a polyvinylidene fluoride membrane (Millipore). The blots were incubated for 2 hours at room temperature in a blocking solution (pH 7.4) containing 20 mM tris-HCl, 137 mM NaCl, 0.1% Tween 20 (TBST) and 5% nonfat milk and then in the same solution containing the antibody against melanopsin (PA1-780, 1:500; Thermo Fisher Scientific) overnight at 4°C. β-Actin (A5541, 1:5000; Sigma-Aldrich) was used as loading control. After that, the blots were washed three times for 10 min by TBST, followed by incubating in horseradish peroxidase–conjugated donkey anti-rabbit IgG secondary antibody (ab6802, 1:2000; Abcam, UK) for 2 hours at room temperature and washed again. The immunosignals were visualized with enhanced chemiluminescence (34096, Thermo Fisher Scientific) and analyzed on ChemiDoc XRS System with Image Lab software (Bio-Rad, USA).

Wheel-running activity

Wheel-running activity was recorded with wireless running wheel systems (ENV-047, MED Associates Inc., USA) equipped with a sensor hub (DIG-807, MED Associates Inc.). The voluntary activities of mice injected with MEL-SAP and PBS in left and right eyes, respectively, and of those with PBS injected in both eyes were monitored. In a room with a timer-controlled independent illuminating system, mice were housed individually in a cage with a running wheel. They were first maintained at 12:12-hour LD cycle for 3 weeks for adaptation to the environment. Subsequently, their activities under 12:12-hour LD, DD, and LL conditions were recorded for 2 weeks each. Actograms were generated and analyzed by Running Wheel Manger software (SOF-860, MED Associates Inc.) and online circadian software (www.circadian.org).

Electroretinographic recording

ERG was recorded with a custom-made system (*39*). After overnight dark adaptation, mice were anesthetized by intraperitoneal injection of 0.6% pentobarbital sodium (10 μl/g body weight) under weak red light. Compound tropicamide eye drops (Mydrin-p; Santen Pharmaceutical, Japan) were gently dropped onto the eyes to dilate pupils. During the experiments, eyes were kept moist with sterile saline. Gold wire ring electrodes (3104RC; Roland, Germany) were placed on the surface of corneas to record ERG responses from both eyes, and needle electrodes were placed in the cheek and tail as reference and ground leads, respectively. In a custom-built Ganzfeld dome, eyes were stimulated by 3-ms white light flashes (6000 K in color temperature) provided by a light-emitting diode (LED) light source (CQ-LU9079; Qianhan Lighting, China) at two different intensities: 5×0.01 cd·s/m^2 for evoking rod-dominant responses, followed by 5×3 cd·s/m^2 for evoking mixed rod- and cone-driven responses. ERG responses were amplified with a preamplifier (FZG-81; Jia Long Educational Instruments, China), band-pass–filtered at 0.1 to 100 Hz, and digitized at 2 kHz. Data recorded were analyzed by a custom-texted program in LabVIEW (National Instruments, USA). Amplitudes of a-waves were calculated by subtracting the baseline from the peak, whereas amplitudes of b-waves were measured from the baseline (responses without a-waves) or the proceeding troughs (responses with a-waves). Final amplitudes of each eye were averaged from calculations of five times recordings.

Pupillometry

Pupillometry was done in *Opn4*$^{Cre/+}$ mice at 3 weeks after AAV-hSyn-DIO-hM3Dq-GFP injection. Before the experiment, animals were dark-adapted for at least 12 hours. Measurements were started in the daytime, typically at 09:00 a.m. Under dim red illumination, the mouse was placed in a head-and-body restrainer with a metal bar (implanted into the skull 2 days before the recording) fixed to the restrainer. Pupil images were recorded at different time points (right before and 30, 60, 120, 150, 180, 210, 240, 270, 300, 330, 360, 390, 420, 450, 480, 510, 540, 570, 600, 630, 660, and 690 min after CNO injection) using a pupilometer (A2000; Neuroptics Inc., USA) in combination with Bandicam software (Bandicam Company, South Korea) under infrared light and further analyzed with ImageJ

software. Percentage pupil constrictions were calculated as the pupil areas at different post-CNO injection time points relative to that before CNO administration.

MEA recording

Retinal preparation

C57BL/6 mice treated with 4-week form deprivation were sacrificed by spinal dislocation after dark-adapted overnight. Under dim red light, the eyes were enucleated immediately and put into Ames' medium (A1420, Sigma-Aldrich), which was equilibrated with 95% O_2 and 5% CO_2. Retinas were dissected from the eyecups and mounted onto a piece of anodisc filter membrane (Anodisc 25, GE Health Bio-Sciences, USA) with photoreceptor side down. Mounted retinas were transferred into the recording chamber of a MEA chip (60MEA200/30iR-ITO-gr, Multi Channel Systems, Germany) with ganglion cell side toward the array and then continuously perfused with oxygenated Ames' medium with the help of an ismatec peristaltic pump (78023-00, Cole-Parmer, USA) and maintained at 30° ± 2°C using a temperature controller (TC-324B, Warner Instruments, USA).

Data acquisition and light stimulation

Data acquisition was performed using the USB-MEA60-Inv-BC-System and MC_Rack software (Multi Channel Systems) when the retina preparation was placed in a light-tight Faraday cage. Raw electrical signals were amplified, digitized at 10 kHz, high-pass–filtered at 200 Hz, and written to disk of a Dell PC. Retinas were full-field stimulated by 10-s 480-nm light flashes generated using a custom-modified fiber optic LED illuminator (ScopeLED Model 66991, Dicon Fiberoptics, USA) with stimulus timing controlled by a logic circuit integrated in the illuminator. Light intensities (3.42×10^{11} to 1.51×10^{15} photons cm^{-2} s^{-1}) were adjusted by a neutral density filter kit (66155, Edmund Optics Inc., USA) introduced to the light path. Stimuli were presented in a series that was monotonically ascending in intensity and identical for all experiments. Interstimulus intervals increased by 0.5 log unit steps progressively, ranging from 5 min between dim stimuli to 10 min between the brightest stimuli. Melanopsin-based ipRGC responses were identified by the sluggish, persistent spiking in the presence of a glutamatergic blocker cocktail, which consisted of 50 μM L-AP4 (group III metabotropic glutamate receptor agonist, Tocris), 40 μM DNQX (AMPA/kainate receptor antagonist, Tocris), 30 μM D-AP5 (*N*-methyl-D-aspartate receptor antagonist, Tocris), and 2 μM ACET (kainate receptor antagonist, Tocris).

Spike sorting and data analysis

Spike sorting of the raw recording data followed a protocol previously described using Offline Sorter software (Plexon Inc., USA) with manual correction for clustering errors (*29*). The resulting timestamps of individual ipRGCs were further processed with OriginPro 2017 (OriginLab Corp., USA) and Microsoft Excel (Microsoft Corporation, USA) to measure two major parameters of light responses: total spike number during light stimulus and peak latency (the interval between light onset and the time point when peak firing rate occurred).

Specific ablation of M1 ipRGCs

P21 *Opn4*$^{Cre/+}$ mice were deeply anesthetized by intraperitoneal injection of 0.6% pentobarbital sodium (10 μl/g body weight). AAV-EF1α-DIO-Flp (2 μl; BrainVTA) was injected into left eyes with a Nanoject II microinjector, while 2 μl of AAV-EF1α-DIO-mCherry (BrainVTA) was injected into right eyes as controls. Immediately after the intravitreal injection, the mice received stereotaxic injection as previously described (*64*). In brief, after skull fur was shaved, the head of the mouse was mounted in a stereotaxic frame and the surgical site was sterilized with iodophor and 75% ethanol. Small holes over bilateral POA and PHb were drilled, and a glass micropipette was inserted into bilateral POA and PHb sequentially to inject 200 nl of AAV-retro-EF1α-fDIO-DTA (BrainVTA) to each site with a glass micropipette (tip diameter of 10 to 30 μm) controlled by an air pressure system (WPI Micro 4, RWD, China). All viral vectors used were at a titer of $>2 \times 10^{12}$ vg/ml.

High-performance liquid chromatography

Because DA contents in the C57BL/6 mouse retina undergo diurnal fluctuation, all retinal and vitreous samples were collected at zeitgeber time 1 (1 hour into the light period), when retinal DA levels reach the daily peak (*65*). Ten weeks after injections of MEL-SAP and PBS, mice were sacrificed by spinal dislocation. Retinas and vitreous bodies (collected using an Eppendorf pipette with a 10-μl pipette tip) were harvested quickly and added into 100 and 15 μl of ice-cold 0.1 M perchloric acid (containing 10 μM ascorbic acid, 0.1 mM EDTA disodium salt, and 0.02 μM 3,4-dihydroxybenzylamine), respectively. DA and DOPAC levels were assessed with an Agilent 1200 series neurotransmitter analyzer (Agilent Technologies, USA) as previously reported (*39*). The data were collected and analyzed by ChemStation (Agilent Technologies).

Statistical analysis

Data are presented as means ± SEM. All statistical analyses were performed with OriginPro 2017 and GraphPad Prism 8 (GraphPad Software). Before ANOVA, a one-sample Kolmogorov-Smirnov test was done with all data groups to verify whether they were distributed normally. Statistical significance between two eyes of the same animal was determined by paired *t* test, whereas unpaired *t* test or one-way ANOVA was applied when comparing eyes from different mice. Difference in growth curves and that in I-R curves were compared with two-way ANOVA followed with Sidak post hoc multiple comparisons tests. Significant difference was defined as a *P* value smaller than 0.05.

SUPPLEMENTARY MATERIALS

Supplementary material for this article is available at https://science.org/doi/10.1126/sciadv.abm9027

View/request a protocol for this paper from *Bio-protocol*.

REFERENCES AND NOTES

1. J. Wallman, J. Winawer, Homeostasis of eye growth and the question of myopia. *Neuron* **43**, 447–468 (2004).
2. I. G. Morgan, K. Ohno-Matsui, S.-M. Saw, Myopia. *Lancet* **379**, 1739–1748 (2012).
3. P. N. Baird, S. M. Saw, C. Lanca, J. A. Guggenheim, E. L. Smith Iii, X. Zhou, K. O. Matsui, P. C. Wu, P. Sankaridurg, A. Chia, M. Rosman, E. L. Lamoureux, R. Man, M. He, Myopia. *Nat. Rev. Dis. Primers* **6**, 99 (2020).
4. D. P. Crewther, The role of photoreceptors in the control of refractive state. *Prog. Retin. Eye Res.* **19**, 421–457 (2000).
5. D. M. Berson, F. A. Dunn, M. Takao, Phototransduction by retinal ganglion cells that set the circadian clock. *Science* **295**, 1070–1073 (2002).
6. S. Hattar, H. W. Liao, M. Takao, D. M. Berson, K. W. Yau, Melanopsin-containing retinal ganglion cells: Architecture, projections, and intrinsic photosensitivity. *Science* **295**, 1065–1070 (2002).
7. M. L. Aranda, T. M. Schmidt, Diversity of intrinsically photosensitive retinal ganglion cells: Circuits and functions. *Cell. Mol. Life Sci.* **78**, 889–907 (2021).
8. L. E. Quattrochi, M. E. Stabio, I. Kim, M. C. Ilardi, P. Michelle Fogerson, M. L. Leyrer, D. M. Berson, The M6 cell: A small-field bistratified photosensitive retinal ganglion cell. *J. Comp. Neurol.* **527**, 297–311 (2019).

9. D. Goz, K. Studholme, D. A. Lappi, M. D. Rollag, I. Provencio, L. P. Morin, Targeted destruction of photosensitive retinal ganglion cells with a saporin conjugate alters the effects of light on mouse circadian rhythms. *PLOS ONE* **3**, e3153 (2008).
10. A. D. Guler, J. L. Ecker, G. S. Lall, S. Haq, C. M. Altimus, H. W. Liao, A. R. Barnard, H. Cahill, T. C. Badea, H. Zhao, M. W. Hankins, D. M. Berson, R. J. Lucas, K. W. Yau, S. Hattar, Melanopsin cells are the principal conduits for rod-cone input to non-image-forming vision. *Nature* **453**, 102–105 (2008).
11. M. Hatori, H. Le, C. Vollmers, S. R. Keding, N. Tanaka, C. Schmedt, T. Jegla, S. Panda, Inducible ablation of melanopsin-expressing retinal ganglion cells reveals their central role in non-image forming visual responses. *PLOS ONE* **3**, e2451 (2008).
12. A. E. Allen, F. P. Martial, R. J. Lucas, Form vision from melanopsin in humans. *Nat. Commun.* **10**, 2274 (2019).
13. R. J. Lucas, A. E. Allen, N. Milosavljevic, R. Storchi, T. Woelders, Can we see with melanopsin? *Annu. Rev. Vis. Sci.* **6**, 453–468 (2020).
14. K. B. Sondereker, M. E. Stabio, J. M. Renna, Crosstalk: The diversity of melanopsin ganglion cell types has begun to challenge the canonical divide between image-forming and non-image-forming vision. *J. Comp. Neurol.* **528**, 2044–2067 (2020).
15. R. A. Stone, W. Wei, S. Sarfare, B. McGeehan, K. C. Engelhart, T. S. Khurana, M. G. Maguire, P. M. Iuvone, D. L. Nickla, Visual image quality impacts circadian rhythm-related gene expression in retina and in choroid: A potential mechanism for ametropias. *Invest. Ophthalmol. Vis. Sci.* **61**, 13 (2020).
16. L. He, M. R. Frost, J. T. Siegwart Jr., T. T. Norton, Altered gene expression in tree shrew retina and retinal pigment epithelium produced by short periods of minus-lens wear. *Exp. Eye Res.* **168**, 77–88 (2018).
17. L. Huang, T. Yuan, M. Tan, Y. Xi, Y. Hu, Q. Tao, Z. Zhao, J. Zheng, Y. Han, F. Xu, M. Luo, P. J. Sollars, M. Pu, G. E. Pickard, K. F. So, C. Ren, A retinoraphe projection regulates serotonergic activity and looming-evoked defensive behaviour. *Nat. Commun.* **8**, 14908 (2017).
18. S. Panda, T. K. Sato, A. M. Castrucci, M. D. Rollag, W. J. DeGrip, J. B. Hogenesch, I. Provencio, S. A. Kay, Melanopsin (Opn4) requirement for normal light-induced circadian phase shifting. *Science* **298**, 2213–2216 (2002).
19. N. F. Ruby, T. J. Brennan, X. Xie, V. Cao, P. Franken, H. C. Heller, B. F. O'Hara, Role of melanopsin in circadian responses to light. *Science* **298**, 2211–2213 (2002).
20. D. L. Nickla, Ocular diurnal rhythms and eye growth regulation: Where we are 50 years after Lauber. *Exp. Eye Res.* **114**, 25–34 (2013).
21. R. A. Stone, A. M. McGlinn, R. Chakraborty, D. C. Lee, V. Yang, A. Elmasri, E. Landis, J. Shaffer, P. M. Iuvone, X. Zheng, A. Sehgal, M. T. Pardue, Altered ocular parameters from circadian clock gene disruptions. *PLOS ONE* **14**, e0217111 (2019).
22. N. Milosavljevic, J. Cehajic-Kapetanovic, C. A. Procyk, R. J. Lucas, Chemogenetic activation of melanopsin retinal ganglion cells induces signatures of arousal and/or anxiety in mice. *Curr. Biol.* **26**, 2358–2363 (2016).
23. W. T. Keenan, A. C. Rupp, R. A. Ross, P. Somasundaram, S. Hiriyanna, Z. Wu, T. C. Badea, P. R. Robinson, B. B. Lowell, S. S. Hattar, A visual circuit uses complementary mechanisms to support transient and sustained pupil constriction. *eLife* **5**, e15392 (2016).
24. J. W. Mouland, F. P. Martial, R. J. Lucas, T. M. Brown, Modulations in irradiance directed at melanopsin, but not cone photoreceptors, reliably alter electrophysiological activity in the suprachiasmatic nucleus and circadian behaviour in mice. *J. Pineal Res.* **70**, e12735 (2021).
25. J. L. Ecker, O. N. Dumitrescu, K. Y. Wong, N. M. Alam, S. K. Chen, T. LeGates, J. M. Renna, G. T. Prusky, D. M. Berson, S. Hattar, Melanopsin-expressing retinal ganglion-cell photoreceptors: Cellular diversity and role in pattern vision. *Neuron* **67**, 49–60 (2010).
26. R. J. Lucas, S. Hattar, M. Takao, D. M. Berson, R. G. Foster, K. W. Yau, Diminished pupillary light reflex at high irradiances in melanopsin-knockout mice. *Science* **299**, 245–247 (2003).
27. R. J. Lucas, M. S. Freedman, M. Muñoz, J. M. Garcia-Fernández, R. G. Foster, Regulation of the mammalian pineal by non-rod, non-cone, ocular photoreceptors. *Science* **284**, 505–507 (1999).
28. B. Lin, E. B. Peng, Retinal ganglion cells are resistant to photoreceptor loss in retinal degeneration. *PLOS ONE* **8**, e68084 (2013).
29. S. Weng, M. E. Estevez, D. M. Berson, Mouse ganglion-cell photoreceptors are driven by the most sensitive rod pathway and by both types of cones. *PLOS ONE* **8**, e66480 (2013).
30. D. C. Tu, D. Zhang, J. Demas, E. B. Slutsky, I. Provencio, T. E. Holy, R. N. Van Gelder, Physiologic diversity and development of intrinsically photosensitive retinal ganglion cells. *Neuron* **48**, 987–999 (2005).
31. W. Zhou, L. Q. Wang, Y. Q. Shao, X. Han, C. X. Yu, F. Yuan, X. Wang, S. J. Weng, Y. M. Zhong, X. L. Yang, Orexin-A intensifies mouse pupillary light response by modulating intrinsically photosensitive retinal ganglion cells. *J. Neurosci.* **41**, 2566–2580 (2021).
32. W. Y. Chen, X. Han, L. J. Cui, C. X. Yu, W. L. Sheng, J. Yu, F. Yuan, Y. M. Zhong, X. L. Yang, S. J. Weng, Cell-subtype-specific remodeling of intrinsically photosensitive retinal ganglion cells in streptozotocin-induced diabetic mice. *Diabetes* **70**, 1157–1169 (2021).
33. Z. Zhang, C. Beier, T. Weil, S. Hattar, The retinal ipRGC-preoptic circuit mediates the acute effect of light on sleep. *Nat. Commun.* **12**, 5115 (2021).
34. K. An, H. Zhao, Y. Miao, Q. Xu, Y. F. Li, Y. Q. Ma, Y. M. Shi, J. W. Shen, J. J. Meng, Y. G. Yao, Z. Zhang, J. T. Chen, J. Bao, M. Zhang, T. Xue, A circadian rhythm-gated subcortical pathway for nighttime-light-induced depressive-like behaviors in mice. *Nat. Neurosci.* **23**, 869–880 (2020).
35. X. Zhou, M. T. Pardue, P. M. Iuvone, J. Qu, Dopamine signaling and myopia development: What are the key challenges. *Prog. Retin. Eye Res.* **61**, 60–71 (2017).
36. M. Feldkaemper, F. Schaeffel, An updated view on the role of dopamine in myopia. *Exp. Eye Res.* **114**, 106–119 (2013).
37. C. L. Prigge, P. T. Yeh, N. F. Liou, C. C. Lee, S. F. You, L. L. Liu, D. S. McNeill, K. S. Chew, S. Hattar, S. K. Chen, D. Q. Zhang, M1 ipRGCs influence visual function through retrograde signaling in the retina. *J. Neurosci.* **36**, 7184–7197 (2016).
38. M. A. Bergen, H. N. Park, R. Chakraborty, E. G. Landis, C. Sidhu, L. He, P. M. Iuvone, M. T. Pardue, Altered refractive development in mice with reduced levels of retinal dopamine. *Invest. Ophthalmol. Vis. Sci.* **57**, 4412–4419 (2016).
39. X. H. Wu, K. W. Qian, G. Z. Xu, Y. Y. Li, Y. Y. Ma, F. Huang, Y. Q. Wang, X. Zhou, J. Qu, X. L. Yang, Y. M. Zhong, S. J. Weng, The role of retinal dopamine in C57BL/6 mouse refractive development as revealed by intravitreal administration of 6-hydroxydopamine. *Invest. Ophthalmol. Vis. Sci.* **57**, 5393–5404 (2016).
40. R. Chakraborty, E. G. Landis, R. Mazade, V. Yang, R. Strickland, S. Hattar, R. A. Stone, P. M. Iuvone, M. T. Pardue, Melanopsin modulates refractive development and myopia. *Exp. Eye Res.* **214**, 108866 (2022).
41. M. T. H. Do, Melanopsin and the intrinsically photosensitive retinal ganglion cells: Biophysics to behavior. *Neuron* **104**, 205–226 (2019).
42. N. Milosavljevic, R. Storchi, C. G. Eleftheriou, A. Colins, R. S. Petersen, R. J. Lucas, Photoreceptive retinal ganglion cells control the information rate of the optic nerve. *Proc. Natl. Acad. Sci. U.S.A.* **115**, E11817–E11826 (2018).
43. D. M. Berson, A. M. Castrucci, I. Provencio, Morphology and mosaics of melanopsin-expressing retinal ganglion cell types in mice. *J. Comp. Neurol.* **518**, 2405–2422 (2010).
44. O. Dkhissi-Benyahya, C. Coutanson, K. Knoblauch, H. Lahouaoui, V. Leviel, C. Rey, M. Bennis, H. M. Cooper, The absence of melanopsin alters retinal clock function and dopamine regulation by light. *Cell. Mol. Life Sci.* **70**, 3435–3447 (2013).
45. T. J. Viney, K. Balint, D. Hillier, S. Siegert, Z. Boldogkoi, L. W. Enquist, M. Meister, C. L. Cepko, B. Roska, Local retinal circuits of melanopsin-containing ganglion cells identified by transsynaptic viral tracing. *Curr. Biol.* **17**, 981–988 (2007).
46. R. J. Lucas, G. S. Lall, A. E. Allen, T. M. Brown, How rod, cone, and melanopsin photoreceptors come together to enlighten the mammalian circadian clock. *Prog. Brain Res.* **199**, 1–18 (2012).
47. M. He, F. Xiang, Y. Zeng, J. Mai, Q. Chen, J. Zhang, W. Smith, K. Rose, I. G. Morgan, Effect of time spent outdoors at school on the development of myopia among children in China: A randomized clinical trial. *JAMA* **314**, 1142–1148 (2015).
48. S. Chen, Z. Zhi, Q. Ruan, Q. Liu, F. Li, F. Wan, P. S. Reinach, J. Chen, J. Qu, X. Zhou, Bright light suppresses form-deprivation myopia development with activation of dopamine D1 receptor signaling in the ON pathway in retina. *Invest. Ophthalmol. Vis. Sci.* **58**, 2306–2316 (2017).
49. A. N. French, R. S. Ashby, I. G. Morgan, K. A. Rose, Time outdoors and the prevention of myopia. *Exp. Eye Res.* **114**, 58–68 (2013).
50. D. Q. Zhang, K. Y. Wong, P. J. Sollars, D. M. Berson, G. E. Pickard, D. G. McMahon, Intraretinal signaling by ganglion cell photoreceptors to dopaminergic amacrine neurons. *Proc. Natl. Acad. Sci. U.S.A.* **105**, 14181–14186 (2008).
51. S. N. Qiao, Z. Zhang, C. P. Ribelayga, Y. M. Zhong, D. Q. Zhang, Multiple cone pathways are involved in photic regulation of retinal dopamine. *Sci. Rep.* **6**, 28916 (2016).
52. A. Delwig, S. Y. Chaney, A. S. Bertke, J. Verweij, S. Quirce, D. D. Larsen, C. Yang, E. Buhr, R. VAN Gallar, J. Gallar, T. Margolis, D. R. Copenhagen, Melanopsin expression in the cornea. *Vis. Neurosci.* **35**, E004 (2018).
53. A. Matynia, S. Parikh, N. Deot, A. Wong, P. Kim, S. Nusinowitz, M. B. Gorin, Light aversion and corneal mechanical sensitivity are altered by intrinscally photosensitive retinal ganglion cells in a mouse model of corneal surface damage. *Exp. Eye Res.* **137**, 57–62 (2015).
54. A. A. Vugler, P. Redgrave, M. Semo, J. Lawrence, J. Greenwood, P. J. Coffey, Dopamine neurones form a discrete plexus with melanopsin cells in normal and degenerating retina. *Exp. Neurol.* **205**, 26–35 (2007).
55. X. H. Wu, Y. Y. Li, P. P. Zhang, K. W. Qian, J. H. Ding, G. Hu, S. J. Weng, X. L. Yang, Y. M. Zhong, Unaltered retinal dopamine levels in a C57BL/6 mouse model of form-deprivation myopia. *Invest. Ophthalmol. Vis. Sci.* **56**, 967–977 (2015).
56. M. A. Cameron, N. Pozdeyev, A. A. Vugler, H. Cooper, P. M. Iuvone, R. J. Lucas, Light regulation of retinal dopamine that is independent of melanopsin phototransduction. *Eur. J. Neurosci.* **29**, 761–767 (2009).
57. A. R. Barnard, S. Hattar, M. W. Hankins, R. J. Lucas, Melanopsin regulates visual processing in the mouse retina. *Curr. Biol.* **16**, 389–395 (2006).

58. S. Sekaran, D. Lupi, S. L. Jones, C. J. Sheely, S. Hattar, K. W. Yau, R. J. Lucas, R. G. Foster, M. W. Hankins, Melanopsin-dependent photoreception provides earliest light detection in the mammalian retina. *Curr. Biol.* **15**, 1099–1107 (2005).
59. S. Weng, K. Y. Wong, D. M. Berson, Circadian modulation of melanopsin-driven light response in rat ganglion-cell photoreceptors. *J. Biol. Rhythms* **24**, 391–402 (2009).
60. F. Caval-Holme, Y. Zhang, M. B. Feller, Gap junction coupling shapes the encoding of light in the developing retina. *Curr. Biol.* **29**, 4024–4035.e5 (2019).
61. G. Sikka, G. P. Hussmann, D. Pandey, S. Cao, D. Hori, J. T. Park, J. Steppan, J. H. Kim, V. Barodka, A. C. Myers, L. Santhanam, D. Nyhan, M. K. Halushka, R. C. Koehler, S. H. Snyder, L. A. Shimoda, D. E. Berkowitz, Melanopsin mediates light-dependent relaxation in blood vessels. *Proc. Natl. Acad. Sci. U.S.A.* **111**, 17977–17982 (2014).
62. N. Zhang, T. L. Favazza, A. M. Baglieri, I. Y. Benador, E. R. Noonan, A. B. Fulton, R. M. Hansen, P. M. Iuvone, J. D. Akula, The rat with oxygen-induced retinopathy is myopic with low retinal dopamine. *Invest. Ophthalmol. Vis. Sci.* **54**, 8275–8284 (2013).
63. F. Schaeffel, E. Burkhardt, H. C. Howland, R. W. Williams, Measurement of refractive state and deprivation myopia in two strains of mice. *Optom. Vis. Sci.* **81**, 99–110 (2004).
64. H. Luo, H. Z. Liu, W. W. Zhang, M. Matsuda, N. Lv, G. Chen, Z. Z. Xu, Y. Q. Zhang, Interleukin-17 regulates neuron-glial communications, synaptic transmission, and neuropathic pain after chemotherapy. *Cell Rep.* **29**, 2384–2397.e5 (2019).
65. S. E. Doyle, M. S. Grace, W. McIvor, M. Menaker, Circadian rhythms of dopamine in mouse retina: The role of melatonin. *Vis. Neurosci.* **19**, 593–601 (2002).

Acknowledgments: We thank S. Hattar (National Institute of Mental Health) for providing the *Opn4*$^{Cre/Cre}$ and *Opn4*$^{Cre/+}$ mice; T. Xue (University of Science and Technology of China) for the gift of *Opn4*$^{-/-}$ and *rd/rd cl* mice; X. Zhou, Y. Zeng, and F. Huang (Wenzhou Medical University) for SD-OCT data collection; W. Dong (Southwest Medical University) for providing the PA1-780 antibody; G.-Z. Xu (Changchun University of Science and Technology) for insightful discussion; and W.-M. Hu and M. Shen for valuable help with English editing. **Funding:** This work was supported by the National Natural Science Foundation of China (81790640, 82070993, 31571072, 32070989, 31872766, and 31571075), the Ministry of Science and Technology of China (2011CB504602 and 2015AA020512), Shanghai Municipal Science and Technology Major Project (no. 2018SHZDZX01), ZJLab, Shanghai Center for Brain Science and Brain-Inspired Technology, and Sanming Project of Medicine in Shenzhen (SZSM202011015).

Author contributions: Experiment design: S.-J.W. and A.-L.L. Experiment administration: A.-L.L., Y.-F.L., G.W., Y.-Q.S., C.-X.Y., Z.Y., Z.-R.Z., X.H., X.G., K.-W.Q., L.-Q.W., and Y.-Y.M. Data analysis: A.-L.L., Y.-F.L., Y.-M.Z., and S.-J.W. Writing: X.-L.Y., S.-J.W., Y.-M.Z., and A.-L.L.
Competing interests: The authors declare that they have no competing interests. **Data and materials availability:** All data needed to evaluate the conclusions in the paper are present in the paper and/or the Supplementary Materials.

Submitted 20 October 2021
Accepted 19 April 2022
Published 8 June 2022
10.1126/sciadv.abm9027